Quadrupole collectivity in ^{42}Ca from low-energy Coulomb excitation with AGATA

K. Hadyńska-Klęk,[1,2,3,4] P.J. Napiorkowski,[1] M. Zielińska,[5,1] J. Srebrny,[1] A. Maj,[6] F. Azaiez,[7]
J.J. Valiente Dobón,[4] M. Kicińska-Habior,[2] F. Nowacki,[8] H. Naïdja,[8,9,10] B. Bounthong,[8] T. R. Rodríguez,[11]
G. de Angelis,[4] T. Abraham,[1] G. Anil Kumar,[6] D. Bazzacco,[12,13] M. Bellato,[12] D. Bortolato,[12] P. Bednarczyk,[6]
G. Benzoni,[14] L. Berti,[4] B. Birkenbach,[15] B. Bruyneel,[15] S. Brambilla,[14] F. Camera,[14,16] J. Chavas,[5]
B. Cederwall,[17] L. Charles,[8] M. Ciemała,[6] P. Cocconi,[4] P. Coleman-Smith,[18] A. Colombo,[12] A. Corsi,[14,16]
F.C.L. Crespi,[14,16] D.M. Cullen,[19] A. Czermak,[6] P. Désesquelles,[20,21] D.T. Doherty,[5,22] B. Dulny,[6] J. Eberth,[15]
E. Farnea,[12,13] B. Fornal,[6] S. Franchoo,[7] A. Gadea,[23] A. Giaz,[14,16] A. Gottardo,[4] X. Grave,[7] J. Grębosz,[6]
A. Görgen,[3] M. Gulmini,[4] T. Habermann,[9] H. Hess,[15] R. Isocrate,[12,13] J. Iwanicki,[1] G. Jaworski,[1] D.S. Judson,[24]
A. Jungclaus,[25] N. Karkour,[21] M. Kmiecik,[6] D. Karpiński,[2] M. Kisieliński,[1] N. Kondratyev,[26] A. Korichi,[21]
M. Komorowska,[1,2] M. Kowalczyk,[1] W. Korten,[5] M. Krzysiek,[6] G. Lehaut,[27] S. Leoni,[14,16] J. Ljungvall,[21]
A. Lopez-Martens,[21] S. Lunardi,[12,13] G. Maron,[4] K. Mazurek,[6] R. Menegazzo,[12,13] D. Mengoni,[12] E. Merchán,[9,28]
W. Męczyński,[6] C. Michelagnoli,[12,13] J. Mierzejewski,[1] B. Million,[14] S. Myalski,[6] D.R. Napoli,[4] R. Nicolini,[14]
M. Niikura,[7] A. Obertelli,[5] S.F. Özmen,[1] M. Palacz,[1] L. Próchniak,[1] A. Pullia,[14,16] B. Quintana,[29] G. Rampazzo,[4]
F. Recchia,[12,13] N. Redon,[27] P. Reiter,[15] D. Rosso,[4] K. Rusek,[1] E. Sahin,[4] M.-D. Salsac,[5] P.-A. Söderström,[30]
I. Stefan,[7] O. Stézowski,[27] J. Styczeń,[6] Ch. Theisen,[5] N. Toniolo,[4] C.A. Ur,[12,13] V. Vandone,[14,16]
R. Wadsworth,[22] B. Wasilewska,[6] A. Wiens,[15] J.L. Wood,[31] K. Wrzosek-Lipska,[1] and M. Ziębliński[6]

[1] *Heavy Ion Laboratory, University of Warsaw, Pasteura 5A, PL 02-093 Warsaw, Poland*
[2] *Faculty of Physics, University of Warsaw, PL 00-681 Warsaw, Poland*
[3] *Department of Physics, University of Oslo, N-0316 Oslo, Norway*
[4] *INFN Laboratori Nazionali di Legnaro, Viale dell'Università, 2, I-35020 Legnaro, Italy*
[5] *Irfu, CEA, Université Paris-Saclay, F-91191 Gif-sur-Yvette, France*
[6] *Institute of Nuclear Physics, Polish Academy of Sciences, PL 31-342 Kraków, Poland*
[7] *Institut de Physique Nucléaire d'Orsay, F-91400 Orsay, France*
[8] *Université de Strasbourg, IPHC/CNRS, UMR7178, 23 rue du Loess, F-67037 Strasbourg, France*
[9] *GSI Helmholtzzentrum für Schwerionenforschung GmbH, D-64291 Darmstadt, Germany*
[10] *LPMS, Université Constantine 1, Route Ain-El bey, 25000 Constantine, Algérie*
[11] *Universidad Autónoma de Madrid, Departamento de Física Teórica, Madrid, Spain*
[12] *INFN Sezione di Padova, I-35131 Padova, Italy*
[13] *Dipartimento di Fisica e Astronomia dell'Università degli Studi di Padova, I-35131 Padova, Italy*
[14] *Dipartimento di Fisica dell'Università degli Studi di Milano, I-20133 Milano, Italy*
[15] *Institut für Kernphysik, Universität zu Köln, Zülpicher Straße 77, D-50937 Köln, Germany*
[16] *INFN Sezione di Milano, I-20133 Milano, Italy*
[17] *Department of Physics, Royal Institute of Technology, SE-10691 Stockholm, Sweden*
[18] *Daresbury Laboratory, Daresbury, Warrington WA4 4AD, UK*
[19] *Schuster Laboratory, School of Physics and Astronomy,*
The University of Manchester, Manchester, M13 9PL, UK
[20] *Université Paris-Sud, F-91400 Orsay, France*
[21] *Centre de Spectrométrie Nucléaire et de Spectrométrie de Masse (CSNSM/IN2P3/CNRS), F-91405 Orsay, France*
[22] *Department of Physics University of York, Heslington, York, YO10 5DD, UK*
[23] *Instituto de Física Corpuscular IFIC, CSIC-University of Valencia, S-46980 Paterna, Valencia, Spain*
[24] *Oliver Lodge Laboratory, The University of Liverpool, Liverpool, L69 7ZE, UK*
[25] *Instituto de Estructura de la Materia, CSIC, Madrid, E-28006 Madrid, Spain*
[26] *Flerov Laboratory of Nuclear Reactions JINR, RU-141980 Dubna, Russia*
[27] *Universite Lyon 1, CNRS, IN2P3, IPN Lyon, F-69622 Villeurbanne, France*
[28] *Technische Universität Darmstadt, D-64289 Darmstadt, Germany*
[29] *Laboratorio de Radiaciones Ionizantes, Departamento de Física Fundamental, Universidad de Salamanca, Spain*
[30] *Department of Physics and Astronomy, Uppsala University, SE-75120 Uppsala, Sweden*
[31] *School of Physics, Georgia Institute of Technology, Atlanta, Georgia 30332-0430, USA*
(Dated: August 7, 2017)

A Coulomb-excitation experiment to study electromagnetic properties of ^{42}Ca was performed using 170 MeV calcium beam from TANDEM XPU facility at INFN Laboratori Nazionali di Legnaro. Gamma rays from excited states in ^{42}Ca were measured with the AGATA spectrometer. The magnitudes and relative signs of 10 $E2$ matrix elements coupling 6 low-lying states in ^{42}Ca, including the diagonal $E2$ matrix elements of 2_1^+ and 2_2^+ states, were determined using the least-squares code GOSIA. The obtained set of reduced $E2$ matrix elements was analysed using Quadrupole Sum Rule method and yielded overall quadrupole deformation parameters for $0_{1,2}^+$ and $2_{1,2}^+$ states, as well as

asymmetry parameters for $0^+_{1,2}$ states, establishing the coexistence of a weakly-deformed ground-state band and highly-deformed slightly triaxial side band in ^{42}Ca. The experimental results were compared with the state-of-the-art large-scale shell model and beyond-mean-field calculations, which reproduce well the general picture of shape coexistence in ^{42}Ca.

I. INTRODUCTION

Deformation of atomic nuclei is a manifestation of spontaneous symmetry breaking in a quantum many-body system, directly related to collective rotation, which was discovered in molecular physics by Jahn and Teller in 1937 [1]. Nuclear deformation can be related to the shell structure of single-particle levels in a spherical potential and, therefore, the shape evolution in atomic nuclei arises from the competition between the deformation originating from particle-vibration coupling and the pairing correlations stabilizing the nucleus in the potential energy minimum corresponding to the strongly deformed shape.

Superdeformed nuclear shapes were first observed in 1962 through the discovery of a fission isomer in ^{242}Am [2]. Ten years later, the identification of a rotational band in the second minimum of the potential energy surface in ^{240}Pu [3] proved that fission isomers indeed correspond to highly-deformed nuclear shapes. This conclusion was further reinforced by lifetime measurements resulting in typical values of the transitional quadrupole moment $Q_0 \approx 30$ eb [4] for the rotational states built on fission isomers, which corresponds to an axes ratio close to 2:1. Until now, 35 fission isomers have been identified in the actinide region.

In the late 1980s, the first superdeformed high-spin band was discovered in ^{152}Dy [5], followed by observation of very similar structures in other rare-earth nuclei, as well as in A ~ 130 [6, 7] and A ~ 190 [8] mass regions. Such bands appear in the second minimum of the potential energy, created due to the additional energy related to the rotation of a strongly deformed shape. As the depth of the potential well decreases for lower angular momenta, the decay from the second to the first potential minimum usually occurs at spins between around $10\hbar$ and $30\hbar$. The highly fragmented nature of this decay makes it very difficult to establish a firm link between the superdeformed structures and the ground state band, nevertheless, in a few cases this has been possible [9, 10].

The phenomenon of superdeformation thus became a challenge for both experiment and nuclear structure theory, and since then about 300 SD structures have been observed in various regions of the nuclear chart [11]. Transitional quadrupole moments Q_0, measured for these structures, together with those for ground states of even-even nuclei [12], are plotted in Fig. 1. They are expected to provide a good estimate of deformation, as the SD structures behave like rigid rotors, rather weakly coupled to the yrast band in most known cases; it should be noted here that for most non-yrast structures a more sophisticated approach, such as the quadrupole sum rules method presented in the Sec. IV D of the present pa-

per, should be used. The transitional quadrupole moments presented in Fig. 1 were normalised to ZR^2 in order to remove charge dependence, as suggested, for example, in Ref. [13]. The obtained estimates of ground-state deformations, denoted by open circles, follow the $1/A^{1/3}$ dependence away from closed shells, but there are strong deviations from it in the vicinity of closed spherical shells, in particular around ^{208}Pb. The SD bands in the A ~ 150, A ~ 190 and A ~ 230 regions are clearly separated from normal-deformed states due to the superdeformed shell gaps, while those for A<150 span a broad range of deformations and are much closer to the $1/A^{1/3}$ line.

In particular, SD bands have been recently discovered in lighter nuclei (e.g. A~ 60 and lower, see panel b) of Fig. 1), where the number of valence particles is lower as compared to the "traditional" regions of superdeformation, and protons and neutrons may occupy the same orbitals. The value of the quadrupole deformation parameter, β, in the side bands of ^{40}Ca [14, 15], ^{36,38,40}Ar [16–20] and ^{44}Ti [21], as well as ^{35}Cl [22] nuclei is between 0.4 - 0.6, see Tab. I. This is similar to what was previously reported for other mass regions, where superdeformation has been established. However, in contrast to heavier nuclei, strongly deformed bands in A ~ 40 and A ~ 60 isotopes extend to low spins and are linked to other, less deformed states by intense γ-ray transitions.

Considering the relatively small number of nucleons, the A ~ 40 mass region constitutes an excellent testing ground to study the origin of strongly deformed structures within various theoretical approaches. Superdeformation in light nuclei was discussed in the framework of large scale shell model (SM) [23, 24], beyond-mean-field models (BMF) [25–27] and antisymmetrized molecular dynamics (AMD) [28–33]. In particular, the Shell Model was succesful in describing the normal-deformed (ND) and SD structures in ^{40}Ca, with the calculations yielding a spherical ground-state band, a ND band (β=0.3) built on the 0^+_2 state dominated by the $4p-4h$ excitation into the pf shell, and a SD band (β=0.6) built on the 0^+_3 state with an $8p-8h$ configuration [24].

Experimental deformation parameters of known superdeformed bands in the A~ 40 mass region, and their dominant configurations resulting from shell-model calculations are presented in Table I.

In a recent Letter [34] we reported on the results of a dedicated Coulomb excitation experiment to study electromagnetic structure of ^{42}Ca, which provided firm evidence for the superdeformed character of the side band in this nucleus, as well as its slight triaxiality. This result was consistent with the earlier observations sug-
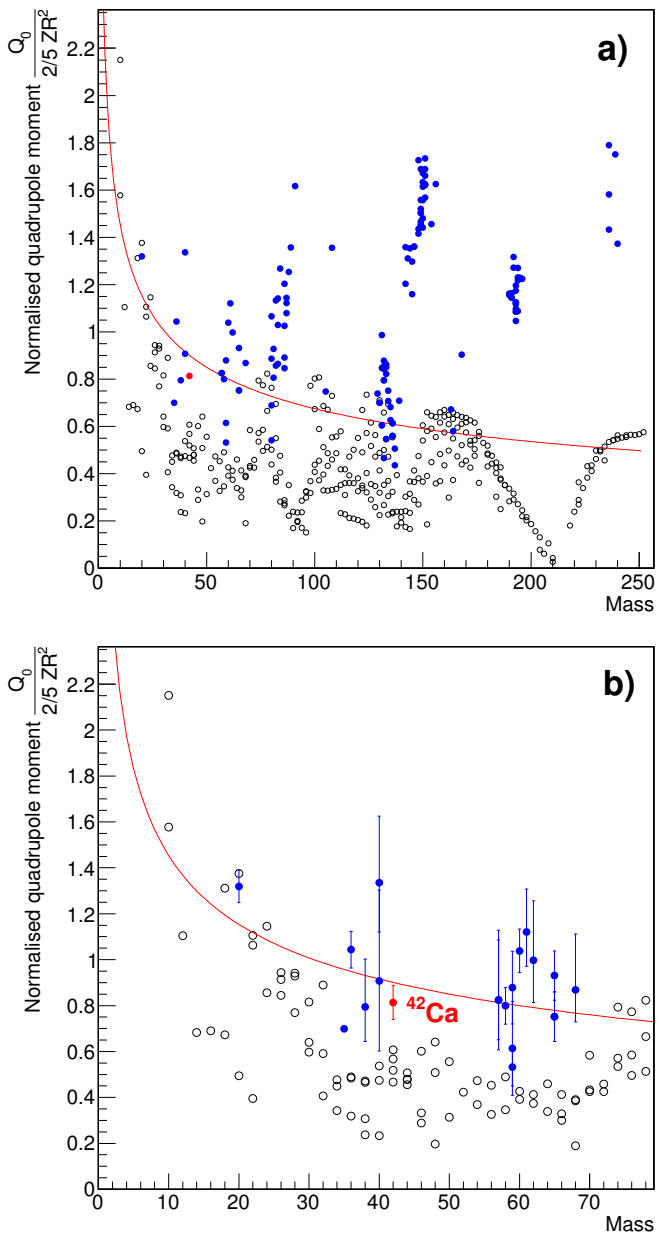
FIG. 1. (Color online) Experimental values of transitional quadrupole moments Q_0, normalised to ZR^2 to remove the Z dependence, for ground-state bands (open circles, [12]), and superdeformed bands (filled circles, [11]). The values for superdeformed bands in the A~ 40 mass region are taken from references listed in Tab. I. The solid line represents the $1/A^{1/3}$ dependence and is scaled to experimental values for mid-shell nuclei. Uncertainties of the values for ground-state bands are not plotted for clarity, as well as those for superdeformed bands in panel a).

gesting a highly-deformed character for this structure. Firstly, its moment of inertia, which is proportional to the quadrupole deformation parameter β_2 [35], is large and similar to those in the SD bands in both ^{36}Ar and ^{40}Ca. Furthermore, this band was preferentially fed by

TABLE I. Experimentally determined β_2 deformation parameters in known superdeformed bands in the A ~ 40 region, and their dominant shell-model configurations.

Isotope	Experimental β_2 value	Configuration
^{40}Ca [14, 15]	$0.59^{+0.11}_{-0.07}$	8p-8h
^{36}Ar [16, 17]	0.42 ± 0.03	4p-8h
^{38}Ar [18, 19]	$0.42^{+0.11}_{-0.08}$	4p-6h
^{40}Ar [20]	$0.48^{+0.16}_{-0.10} \pm 0.05$	4p-4h
^{44}Ti [21]	not known	8p-4h
^{35}Cl [22]	0.37	3p-3h
^{42}Ca [34]	0.43(4) (0_2^+)	6p-4h
	0.45(4) (2_2^+)	6p-4h

the low-energy component of the highly-split giant dipole resonance decay of ^{46}Ti [36]. On the other hand, the band head of the side band in ^{42}Ca lies at excitation energy of 1837 keV, considerably lower than its counter-parts in the neighbouring Ca and Ar isotopes, and so it was possible to populate this structure with Coulomb excitation in order to obtain a complete set of electro-magnetic matrix elements between the observed states. In the present paper we provide a more in-depth description of the experiment, the data analysis procedure and the theoretical calculations. It is organized as follows: the experiments are presented in Sec. II, while the de-tails of of the Coulomb excitation data analysis and the final results are described in Sec. III. In Sec. IV the the-oretical approaches and interpretation are presented. In Sec. IV D the quadrupole sum rules method is introduced and the thus obtained quadrupole shape parameters of the low-lying states in ^{42}Ca are discussed.

II. EXPERIMENTAL DETAILS

A Coulomb-excitation experiment to study the elec-tromagnetic structure and deformation in ^{42}Ca was per-formed at the INFN Laboratori Nazionali di Legnaro, Italy [37, 38].

A continuous ^{42}Ca beam of 170 MeV energy and 1 pnA intensity was delivered by the TANDEM XPU ac-celerator and bombarded a 1-mg/cm^2-thick ^{208}Pb target, enriched to 99%, and a natural ^{197}Au target of the same thickness. The beam energy in both cases was chosen to fulfill Cline's "safe energy" criterion for backscatter-ing [39].

The γ rays from Coulomb excited nuclei were measured with the three triple clusters of AGATA [40] placed at 143.8 mm from the target. The center of AGATA pointed at 63° with respect to the beam direction.

The data were collected requiring coincidence between γ rays and back-scattered ^{42}Ca ions, detected in the DANTE array [41, 42]. This setup consisted of three position-sensitive Micro-Channel Plate (MCP) detectors, of dimensions 40 mm x 60 mm and 13 mm thick, covering

θ_{LAB} angles from $100°$ to $144°$ with respect to the beam direction.

Data acquisition of the AGATA array was fully digital, while signals from the MCP detectors were processed by analog electronics. The readout of DANTE was synchronized and merged with the AGATA acquisition system using the AGAVA interface [40].

The energy and efficiency calibration of the AGATA array in the range up to 2.6 MeV was performed under conditions identical to those in the Coulomb excitation experiment, using ^{152}Eu and ^{226}Ra γ-ray sources placed at the target position. The position calibration of the MCP detectors was performed using an ^{241}Am source and markers placed on the surface of the detectors, as presented in Fig. 2 (upper panel). The two-dimensional particle spectrum of ^{42}Ca particles scattered on the ^{208}Pb target is presented in the bottom panel of Fig. 2.
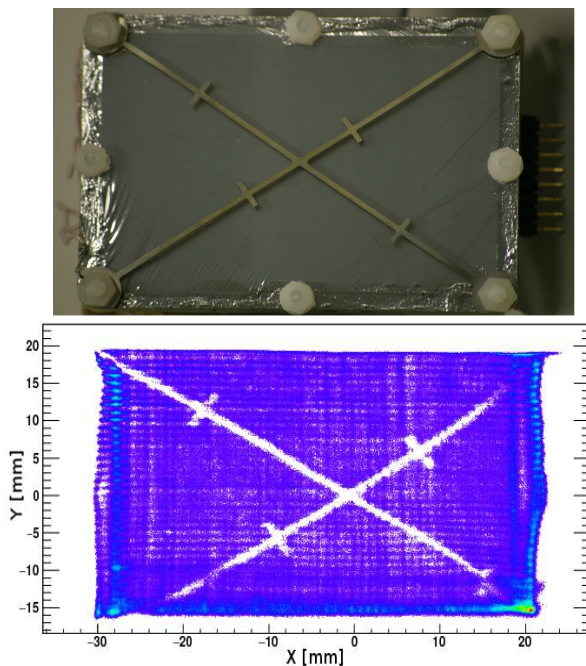

FIG. 2. (Color online) Upper panel: A picture of the MCP detector surface with the markers used for the position calibration. Bottom panel: experimental 2D ^{42}Ca particle spectrum collected with one of the DANTE detectors.

Events were collected with a condition that at least one γ ray was registered in AGATA together with exactly one ^{42}Ca ion detected in one of the MCP detectors within a 400 ns coincidence window. Gates on the particle-γ prompt coincidence peak were set individually for each MCP detector (see Fig. 3).

The kinematic information from the position-sensitive detectors of the DANTE array was used to Doppler correct the energies of γ rays depopulating Coulomb excited states in ^{42}Ca. The γ-ray spectrum obtained with the ^{208}Pb target, Doppler corrected for the ^{42}Ca velocity, in coincidence with back-scattered particles registered
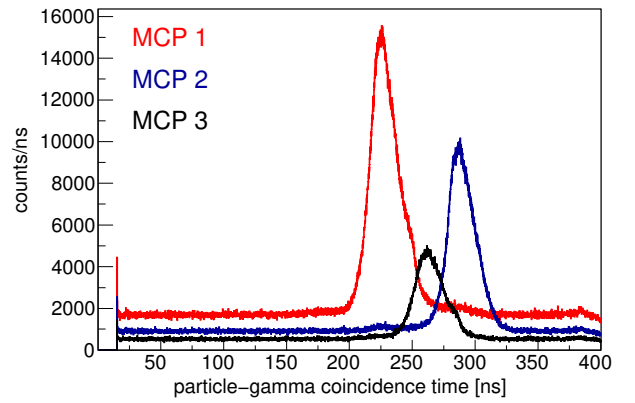

FIG. 3. (Color online) Particle-γ coincidence time spectra for the three MCP detectors of the DANTE array.

in one of the MCP detectors, is shown in Fig. 4. In the experiment the following transitions were observed: $2_1^+ \rightarrow 0_1^+$ (1525 keV), $4_1^+ \rightarrow 2_1^+$ (1227 keV), $2_2^+ \rightarrow 2_1^+$ (899 keV), $2_2^+ \rightarrow 0_1^+$ (2424 keV), $4_2^+ \rightarrow 2_1^+$ (1729 keV) and $0_2^+ \rightarrow 2_1^+$ (312 keV). Their intensities are presented in Table II. Additionally, the excitation of the 6_1^+ state at 3189 keV was observed, but since the lifetime of this state, equal to 7.7(2) ns, is longer than the average time of flight between the target and the particle detector, the weak $6_1^+ \rightarrow 4_1^+$ transition has been completely smeared out when applying Doppler correction.

TABLE II. Numbers of counts in the observed γ-ray transitions in ^{42}Ca, and their relative intensities (corrected for efficiency) normalized to that of the $2_1^+ \rightarrow 0_1^+$ transition.

I_i^π	I_f^π	Energy [keV]	Number of counts	Intensity
			^{208}Pb target	
2_1^+	0_1^+	1525	$1.08\,(8) \times 10^6$	100 (8)
4_1^+	2_1^+	1227	$1.07\,(8) \times 10^4$	0.93 (7)
0_2^+	2_1^+	312	$1.14\,(5) \times 10^5$	6.9 (3)
2_2^+	0_1^+	2424	$2.7\,(7) \times 10^3$	0.28 (8)
4_2^+	2_1^+	1729	$2.9\,(8) \times 10^3$	0.28 (8)
			^{197}Au target	
2_1^+	0_1^+	1525	$9.2\,(8) \times 10^4$	100 (10)
4_1^+	2_1^+	1227	$1.30\,(12) \times 10^3$	1.29 (13)
0_2^+	2_1^+	312	$9.7\,(7) \times 10^3$	6.9 (5)
2_2^+	0_1^+	2424	300 (140)	0.39 (19)
2_2^+	2_1^+	899	$1.12\,(10) \times 10^3$	0.99 (10)
4_2^+	2_1^+	1729	400 (110)	0.45 (13)

A Doppler-broadened and shifted 511-keV γ-ray line, and transitions from Coulomb excitation of target impurities: ^{204}Pb (899 keV), ^{206}Pb (803 keV), ^{207}Pb

(570 keV), are also present in the experimental spectrum. In particular, the Doppler broadened transition in ^{204}Pb obscured the $2^+_2 \rightarrow 2^+_1$ line in ^{42}Ca, and, consequently, the intensity of this transition in data collected using the Pb target could not be included in the Coulomb excitation analysis. The ^{197}Au target was meant to be used mostly to set up proper particle-gamma coincidences, and as a consequence much lower statistics was collected using this target. In this case, however, the 899 keV peak was not contaminated by any transitions resulting from target excitation (see inset of Fig. 4), hence its intensity could be determined with a good precision.
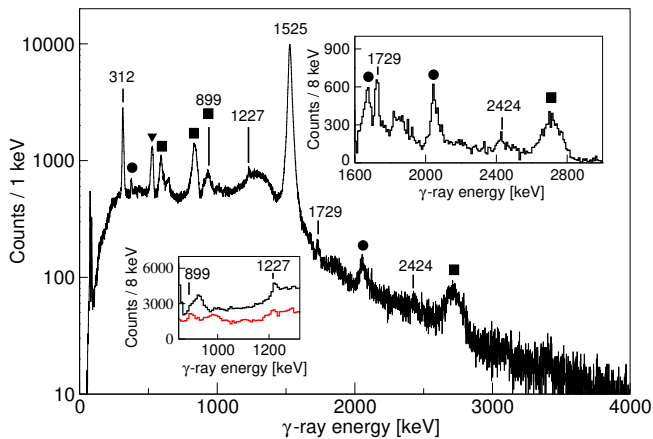

FIG. 4. (Color online) The γ-ray spectrum observed in the ^{42}Ca+^{208}Pb Coulomb excitation experiment in coincidence with back-scattered particles registered in one of MCP detectors, Doppler corrected for the projectile. The lines not originating from ^{42}Ca are marked as follows: ■ – lead isotopes, ▼ – 511 keV, ● – ^{43}Ca. Insets show portions of the spectrum zoomed on the 1600-3000 keV and 850-1300 keV energy ranges, the latter presenting also the spectrum collected with the ^{197}Au target (in red, multiplied by a factor of 3 for presentation purpose). Reproduced from Ref. [34]

A. Sub-barrier transfer reaction

In addition to the transitions resulting from Coulomb excitation of ^{42}Ca and lead isotopes, weaker lines at 376, 1674 and 2048 keV were observed. These could originate from Coulomb excitation of unknown states in ^{42}Ca, or from a different reaction. Both these hypotheses appeared unlikely, as the low-spin part of the level scheme of ^{42}Ca seemed to be well known, and the experiment was performed at a beam energy which did not exceed the strict Cline's "safe energy" criterion [39], thus no processes other than safe Coulomb excitation were likely to occur. However, a 2048-keV transition is present in the decay scheme of ^{43}Ca, related to the deexcitation of the

$p_{3/2}$ single particle state. Two scenarios were therefore tested: that the 376 keV and 2048 keV γ-ray lines resulted from the decay of a Coulomb excited 2^+ state at 2048 keV excitation energy, previously unknown, or that they originated from the ^{208}Pb(^{42}Ca,^{43}Ca)^{207}Pb transfer reaction at about 70% of the Coulomb barrier. Consequently, the angular distribution of the most intense of these γ-ray transitions, 2048 keV, was analysed in order to compare with what would be expected for the sub-barrier neutron transfer reaction ^{208}Pb(^{42}Ca,^{43}Ca)^{207}Pb, and for the Coulomb excitation process. To this end, the range of scattering angles covered by each of the MCP particle detectors was divided into three bins:

- $(105°-114°)$, $(114°-123°)$, $(123°-132°)$ for MCP$^{\#}$1,

- $(111°-120°)$, $(120°-129°)$, $(129°-138°)$ for MCP$^{\#}$2,

- $(118°-126°)$, $(126°-134°)$, $(134°-142°)$ for MCP$^{\#}$3.

Since the B($E2$; $2^+_1 \rightarrow 0^+_1$) value in ^{42}Ca, as well as the spectroscopic quadrupole moment of the 2^+_1 state are well known, it was possible to use this line for normalisation of the measured cross sections: the intensity of the $2^+_1 \rightarrow 0^+_1$ transition, measured for each bin of scattering angle, was compared with the excitation cross section, calculated for the 2^+_1 state using the GOSIA code. The resulting normalisation was applied to the measured intensity of the 2048 keV transition in order to obtain the absolute experimental cross section as a function of scattering angle. Those were compared with the results of two calculations: Coulomb excitation cross section to populate an unknown 2^+ state at 2048 keV, estimated using the GOSIA code, and ^{208}Pb(^{42}Ca,^{43}Ca)^{207}Pb reaction cross section to populate the $p_{3/2}$ state in ^{43}Ca, calculated with a Distorted Wave Born Approximation coupled-reaction-channel code FRESCO [43] (Fig. 5, upper panel).

The observed ratio of the 376- and 2048-keV transition intensities in the present experimental spectra was around 30%, similar to the ratio of the 373- and 2046-keV γ-ray transitions in ^{43}Ca observed in the (d,p) reaction, equal to 32% [44]. The Q value for the ^{208}Pb(^{42}Ca,^{43}Ca)^{207}Pb reaction is positive and equal to 565 keV, supporting the transfer scenario. On the other hand, the angular distribution of the 2048-keV γ line fits better to the Coulomb excitation predictions than to the transfer calculations, as demonstrated in Fig. 5.

Additionally, γ-γ coincidences were analysed. The γ-γ matrix was constructed with the γ rays Doppler corrected for the projectile velocity on one axis, and the γ rays Doppler corrected for the recoil velocity on the other. A coincidence gate set on the 570-keV γ-ray transition deexciting the first excited state in ^{207}Pb showed the 373-
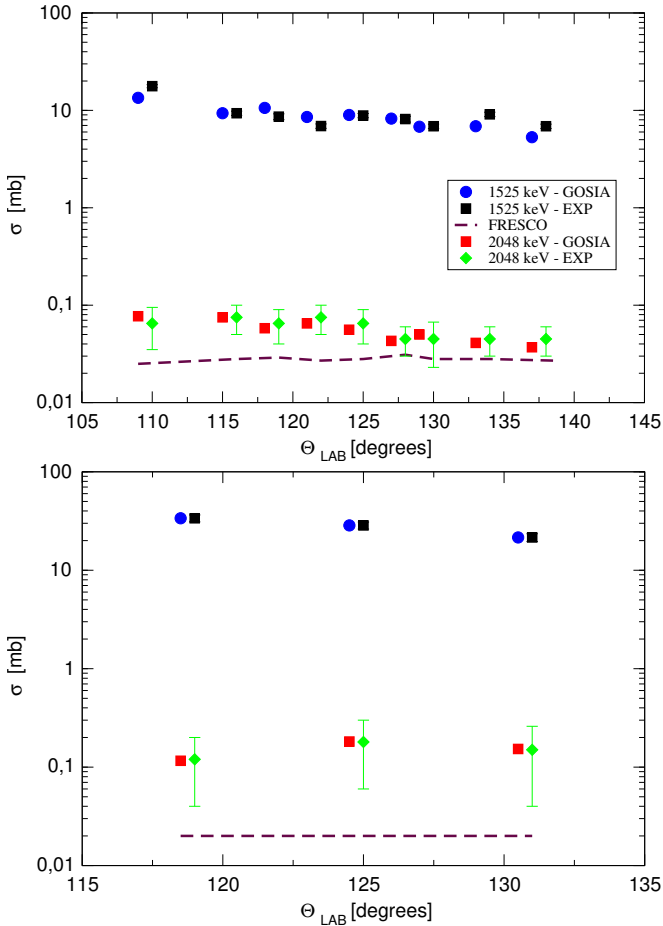
FIG. 5. (Color online) Experimentally measured cross sections compared to the results of calculations with the GOSIA and DWBA codes (FRESCO). Upper panel: ^{42}Ca on ^{208}Pb; bottom panel: ^{42}Ca on ^{197}Au. The points are slightly offset on the x axis for clarity.

keV γ-ray line in ^{43}Ca, as presented on Fig. 6, providing a strong evidence for the one-neutron transfer reaction.

The data collected with the ^{197}Au target were used for a cross check. Although the level of statistics in this measurement was low, it was sufficient to observe the 2048 keV γ transition. Hence, the possibility of one-neutron transfer reaction ^{197}Au(^{42}Ca,^{43}Ca)^{196}Au was taken into consideration, although the Q value is negative (-140 keV). As in the case of data collected with the Pb target, the angular distribution of γ rays related to scattered calcium projectiles was analysed. Due to the lower statistics, the data was subdivided into only three ranges of scattering angles in the laboratory frame:

- $105°$-$132°$ for MCP#1,
- $111°$-$138°$ for MCP#2,
- $118°$-$142°$ for MCP#3.

The bottom panel of Fig. 5 presents again the comparison of experimentally determined cross sections related
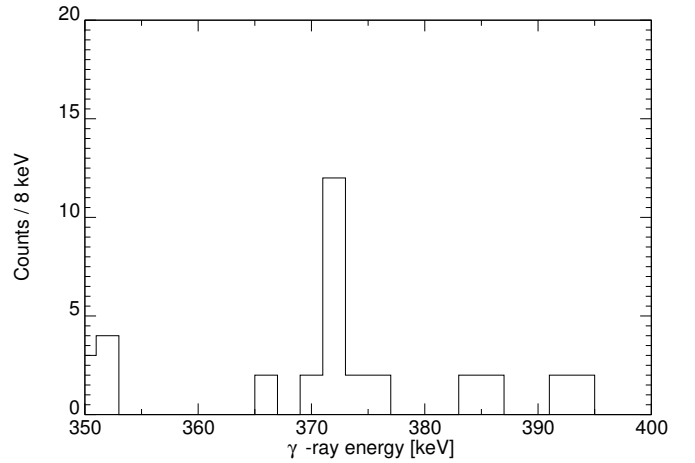

FIG. 6. The $\gamma - \gamma$ spectrum gated on the 570-keV γ-ray transition in ^{207}Pb. The 373-keV γ-ray line originating from ^{43}Ca is shown.

to the 2048-keV transition with the estimates obtained using the GOSIA code and those for the 1n transfer cross section calculated within the DWBA approach. In this case, the experimental 2048-keV γ-ray yields and the cross section calculated using the FRESCO code differ by one order of magnitude. The present DWBA calculations, though, can only be understood as rough estimates, since the relevant optical potentials at the experimental energies and the spectroscopic factors for states in ^{43}Ca and the target nuclei are not precisely known. The angular distributions are in this case more meaningful that the absolute cross sections, and unfortunately, due to the much lower statistics, no conclusion can be drawn from these measured for the ^{197}Au target.

B. Verification of the low-spin structure of ^{42}Ca in a fusion-evaporation experiment

As the measured angular distributions of the 2048-keV transition were better described by Coulomb excitation than by transfer calculations (see Fig. 5), and a presence of an additional state at low excitation energy would influence the results of the Coulomb excitation analysis, it was decided that it would be prudent to perform an experimental verification of the low-spin level scheme of ^{42}Ca. A dedicated fusion-evaporation experiment was performed at the Heavy Ion Laboratory, University of Warsaw [38], using the EAGLE spectrometer [45] consisting of 15 high-purity germanium (HPGe) detectors equipped with anti-Compton BGO shields. Germanium detectors were placed at the following laboratory angles with respect to the beam direction: $25°$ (1 Ge detector), $38°$ (2), $63°$ (2), $90°$ (2), $117°$ (2), $142°$ (2), and $155°$ (1).

A ^{32}S beam of 80 MeV energy bombarded a 100-mg/cm^2 thick ^{12}C target. Significant production of ^{42}Ca was observed in the 2p reaction channel, although it led

mostly to the population of states in the yrast band. The states in the side band in ^{42}Ca, including the 2424-keV level, were populated in the β decay of ^{42}Sc, produced in the *pn* evaporation channel. In its ground state, ^{42}Sc has a half-life of 681.3 ms and J$^\pi$=0$^+$, whereas its isomeric state ^{42}Sc^m has a spin J$^\pi$=7$^+$, and a longer lifetime of T$_{1/2}$ = 61.8 s. ^{42}Sc^m β decays in 100% to the 6$_1^+$ level in ^{42}Ca, which promptly emits three γ rays in a cascade: 437 keV (6$_1^+$ → 4$_1^+$), 1227 keV (4$_1^+$ → 2$_1^+$) and 1524 keV (2$_1^+$ → 0$_1^+$). However, the 4$_1^+$ state at 2752 keV decays also to the 2$_2^+$ state at 2424 keV, with the emission of a 328-keV γ ray. In the experiment, both the 2424- and 899-keV transitions deexciting the 2$_2^+$ state were observed (see Fig. 7), which verified this part of the level scheme of ^{42}Ca and also allowed determination of the branching ratio of the two transitions. The obtained value, 0.35(7), which is in agreement with the previous findings [46, 47], was used to constrain the Coulomb excitation data analysis described in the following Section.
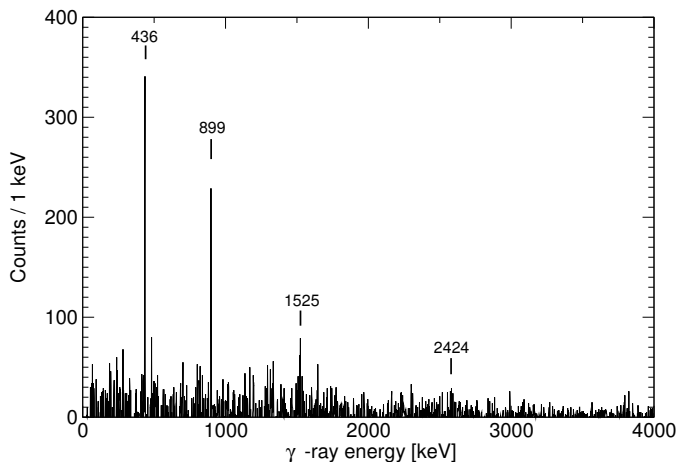

FIG. 7. The γ-ray spectrum collected in ^{12}C+^{32}S experiment, gated at the 328-keV transition deexciting 4$_1^+$ state in ^{42}Ca.

None of the 373-, 1674- and 2046-keV γ-ray transitions present in the Coulomb excitation spectra have been observed in the fusion-evaporation experiment, which provides one more argument to attribute them to one-neutron transfer.

It should be noted that the Cline's criterion [39], fulfilled in the present study, is supposed to ensure that less than 0.5% of the total reaction cross section arises from processes other that safe Coulomb excitation. The ratio of the experimentally measured cross section to populate the p$_{3/2}$ state in ^{43}Ca via the ^{208}Pb(^{42}Ca,^{43}Ca)^{207}Pb transfer reaction, to that to populate the 2$_1^+$ state in Coulomb excitation, is equal to 0.9%. We do not expect that this effect may change the conclusions of the present paper, in particular the $E2$ matrix elements extracted

from the measured transition intensities, as the role of other reaction channels remains negligible as compared to safe Coulomb excitation. It means, however, that for certain combinations of beams and targets the Cline's criterion may not work as well as one might imagine.

III.   COULOMB EXCITATION DATA ANALYSIS

A set of reduced electromagnetic matrix elements between the low-lying states in ^{42}Ca was extracted from the Coulomb-excitation data using the GOSIA code [48, 49]. The level scheme of ^{42}Ca which was considered in the current analysis is presented in Fig. 8. It is known from the following reactions:

- Coulomb excitation [50],

- β decay of ^{42}K [51–53] and ^{42}Sc [54–58],

- reactions induced by heavy ions: ^{28}Si(^{19}F,$p\alpha$)^{42}Ca [59], ^{27}Al(^{18}O,$p2n$)^{42}Ca [60], ^{27}Al(^{19}F,$\alpha\gamma$)^{42}Ca [61], ^{28}Si(^{16}O,$2p\gamma$)^{42}Ca [62–64], ^{40}Ca(^{12}C,^{10}C)^{42}Ca [65],

- reactions induced by light ions: (d,t), (^{3}He,d) and (α,p) [47, 66–71], $(\alpha,2p)$ [72], (t,p) [73],

- elastic and inelastic scattering: (γ,γ') [74], $(p,p'\gamma)$ [46, 75], (d,d') [76].

From the experiments listed above, branching ratios [46, 51, 56, 77] and $E2/M1$ mixing ratios [65, 78] were determined (see Table IV). For the 2$_2^+$ →0$_1^+$/2$_2^+$ →2$_1^+$ branching ratio, the new value determined in the experiment described in Sec. II B was used. Those, together with the known lifetimes of yrast and non-yrast states, summarized in Table III, were used in the GOSIA analysis as additional data points, entering the multidimensional χ^2 fit in the same way as the γ-ray intensities measured in the current Coulomb excitation experiment. This increased the sensitivity to higher-order effects such as spectroscopic quadrupole moments and relative signs of matrix elements, as well as to the influence of non-observed transitions on the measured excitation cross sections, in particular that of the 2$_2^+$ → 0$_2^+$ transition.

For the lifetime of the 2$_1^+$ state at 1525 keV, the value extracted from B($E2;0_1^+$ →2$_1^+$) measured in a one-step Coulomb excitation experiment with a ^{32}S beam [50] was used in the current data analysis. In this measurement, the state of interest was populated from below, and possible influence of multi-step excitation of higher-lying states was well controlled and taken into account in the data analysis. This lifetime was also measured with the Doppler Shift Attenuation Method (DSAM) [71], yielding a value of 0.75(30) ps, but subject to a much larger uncertainty than the Coulomb excitation result [50]. As the sources of possible systematic error seemed to be much
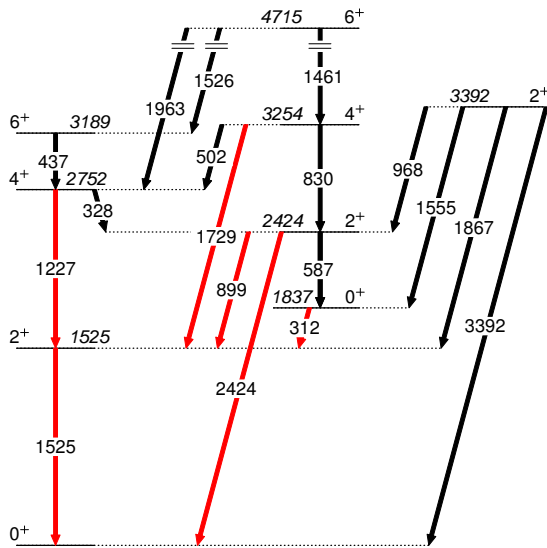
FIG. 8. (Color online) Low-lying excited states in ^{42}Ca, considered in the present analysis. Transitions observed in the current experiment are marked in red. Level and transition energies are given in keV. Reproduced from Ref. [34]

TABLE III. Lifetimes of the excited states in ^{42}Ca used as additional data points in the present Coulomb excitation data analysis.

I_i^π	τ(ps)
2_1^+	1.19 (4)
4_1^+	4.45 (40)
6_1^+	7710 (230)
0_2^+	558 (8)
2_2^+	0.18 (4)
4_2^+	0.18 (3)
6_2^+	0.120 (46)
2_3^+	0.17 (3)

better controlled in the case of the Coulomb excitation experiment [50], the value resulting from the DSAM measurement has not been considered in the current data analysis.

The lifetime of the 4_1^+ state at 2754 keV was measured in several Recoil Distance Method (RDM) experiments following fusion-evaporation reactions, yielding results of 3.8(4) ps [64], 5.1(4) ps [59] 2.3(10) ps [69] and 5.1(4) ps [60]. However, Ref. [59] reported a problem with the feeding of the 4_1^+ state, and consequently the resulting value was not taken into account. Two more existing values were rejected: 3.4(-17,+110) ps and 2.3(10) ps obtained using DSAM in Ref. [46] and in Ref. [69], respectively, because of very large uncertainties, and 11.5(25) ps from a RDM measurement following (α,p) transfer [68], as the authors reported high background due to feeding from the long-lived 6^+ state. In the end, the weighted

average of values obtained in Refs. [64] and [60] was used in the present Coulomb excitation analysis.

The 6_1^+ state at 3189 keV has a much longer lifetime than the other states in ^{42}Ca. In the present data analysis, it was decided to use the weighted average of the values obtained using the differential Perturbed Angular Correlation method (7.65(23) ns, [79]) and positron-γ coincidences (7.96 (22) ns, [58] and 7.76(26) ns, [72]), while the the result of Ref. [71] (7.8(10) ns) was not taken into account because of its much lower precision.

The lifetime of the 0_2^+ state at 1837 keV was determined in a p-γ coincidence measurement [75] to be equal to 558(8) ps. This value had a much smaller uncertainty than that obtained in a delayed β-γ-γ coincidence experiment (480(30) ps, [52]), hence it was used in the current analysis.

For the 2_2^+ state at 2424 keV, a weighted average of the lifetimes determined in two DSAM experiments [46, 71] was used, as they were both performed under similar conditions and the obtained precision was similar (0.30(+3,-4) ps and 0.16(4) ps, respectively).

The lifetime of the 4_2^+ state at 3254 keV was measured in three DSAM experiments [46, 71, 81] under similar experimental conditions, yielding 0.30(+15,-10) ps [46], 0.15(4) ps [71], and 0.18(3) ps [81]. The obtained values agree within error bars, although that reported in Ref. [46] has a considerably lower precision than two later measurements. In the Coulex analysis, the most recent and at the same time most precise value, 0.18(3) ps [81] was used.

The lifetime of the 6_2^+ state at 4715 keV was determined in a DSAM measurement [70] to be equal to 120 (46) fs. The same technique was used to measure the lifetime of the 2_3^+ at 3392 keV equal to 0.17(3) ps [81].

The spectroscopic quadrupole moment of the 2_1^+ state in ^{42}Ca was determined using the reorientation effect in Coulomb excitation [50]. The $2_1^+ \to 0_1^+$ γ-ray intensities, measured for several scattering angles, were analysed using the coupled-channels code of de Boer and Winther [80]. In the calculations, the ground state and states at 1.524 (2_1^+), 1.836 (0_2^+), 2.422 (2_2^+) and 2.75 MeV (4_1^+) were included, with E2 transitional matrix elements taken from Refs. [46, 81].

The 0_2^+ state decays almost exclusively to the 2_1^+ state with the emission of a 312-keV γ ray, however, an electric monopole transition, $0_2^+ \to 0_1^+$, is also known [75, 82–84]. The ratio of $0_2^+ \to 0_1^+/0_2^+ \to 2_1^+$ electron intensities was determined to be equal to 1.03 (10) in a (p,p'γ) study [82]. This is equivalent to the I(E0; $0_2^+ \to 0_1^+$)/I(E2; $0_2^+ \to 2_1^+$) branching of 0.35%. It was decided to include this decay path in the Coulomb excitation data analysis for completeness, even though the effect is small. Since this information cannot be directly introduced into the GOSIA input files, an indirect method described in Ref. [85] was used: an extra level of spin and parity 1^+, at 1200 keV excitation energy, has been declared in addition to the known level scheme of ^{42}Ca, and connected to the 0_2^+

state by a $M1$ transition. The $\langle 1^+ \| M1 \| 0_2^+ \rangle$ was fitted so that the relative intensity of the $0_2^+ \to 1^+$ transition was equal to the relative intensity of E0 electrons measured in Ref. [82]. The introduction of such a level does not affect the observed excitation pattern, as low-energy Coulomb excitation proceeds predominantly via $E2$ transitions; it, however, accounts for the alternative decay path of the 0_2^+ state.

TABLE IV. Relative intensities of the γ transitions and mixing ratios, δ, for mixed $E2/M1$ transitions in ^{42}Ca used as additional data points in the present Coulomb excitation data analysis.

I_i^π	I_j^π	E_γ [keV]	Relative intensity
2_2^+	2_1^+	899	1
2_2^+	0_1^+	2424	0.35(7)
2_2^+	0_2^+	587	0.007(3)
4_1^+	2_1^+	1227	1
4_1^+	2_2^+	328	0.010(4)
4_2^+	2_1^+	1729	1
4_2^+	2_2^+	830	0.18(9)
4_2^+	4_1^+	502	0.64(9)
6_2^+	4_1^+	1963	1
6_2^+	4_2^+	1461	0.94(6)
6_2^+	6_1^+	1526	0.15(4)
2_3^+	2_1^+	1867	1
2_3^+	0_1^+	3392	0.90(6)
2_3^+	0_2^+	1555	0.12(4)
2_3^+	2_2^+	968	0.05(4)
I_i^π	I_j^π	E_γ (keV)	$\delta(E2/M1)$
2_2^+	2_1^+	899	-0.18 (2)
2_3^+	2_1^+	1867	1.7 (4)

In the GOSIA χ^2 fitting procedure, Coulomb excitation amplitudes for all declared states are calculated for a given set of matrix elements and the scattering kinematics, defined by the particle and γ detection geometries. The subsequent calculation of γ-ray decay takes into account effects such as internal conversion, the finite size and relative efficiency of Ge detectors, and the attenuation caused by the deorientation effect during recoil into vacuum. In order to compare the experimentally observed and the calculated γ-ray intensities, the latter are integrated over the range of scattering angles covered by the particle detectors, as well over the range of incident energies due to the beam slowing down in the target material.

The χ^2 fit of the observed γ-ray yields (Tab. II) and other spectroscopic data (Tabs. III and IV) was performed with 26 $E2$ and 4 $M1$ matrix elements.

In particular, although no transitions de-exciting the 2_3^+ state were observed in the present experiment, its influence on the population of other states was taken into account by introducing into the calculations 6 matrix elements coupling it to the observed states. These were calculated from the known spectroscopic data, such as the lifetime of the 2_3^+ state, branching ratios for all possible paths of its decay, and the $2_3^+ \to 2_1^+$ mixing ratio (see Tab. IV), and remained fixed in the GOSIA minimization routine. The $2_3^+ \to 2_2^+$ transition, for which no $E2/M1$ mixing ratio was known, was assumed to be of pure $E2$ character.

The relative signs of matrix elements may have a significant influence on Coulomb excitation cross sections, as illustrated for example by Fig. 3 of Ref. [86]. The signs and magnitudes of the experimental matrix elements reported in the present work were carefully verified by performing the χ^2 minimization procedure starting from different initial sets of matrix elements, and comparing the quality of resulting fits. For example, imposing a positive sign for the $\langle 0_1^+ \| E2 \| 2_2^+ \rangle$ matrix element resulted in an immediate 11-fold increase of the obtained χ^2 value.

The following sign convention has been imposed: sign of all in-band transitional $E2$ matrix elements, both in the ground state band and in the side band, were assumed to be positive, as well as that of $\langle 0_2^+ \| E2 \| 2_1^+ \rangle$. Signs of all other $E2$ matrix elements have been determined relatively to those.

The experiment had no sensitivity to the signs of matrix elements involving the 2_3^+ state; they were assumed to be positive, consistent with the large scale shell model predictions.

The resulting set of reduced matrix elements in ^{42}Ca together with their relative signs and the corresponding B($E2$) values are presented in Table V. In addition, in Tab. VI we present a list of $E2$ and $M1$ matrix elements that were determined from other spectroscopic data, and their values corresponding to the final solution of the GOSIA minimisation procedure.

The statistical errors of the matrix elements were calculated when the convergence of the χ^2 minimization was achieved. This was performed in two steps. Firstly, the χ^2 surface is sampled in the vicinity of the minimum, using different values of the matrix element in question, with all other matrix elements remaining fixed, in order to find the "diagonal" uncertainty. Secondly, possible correlations between all matrix elements are taken into account, in order to obtain the total statistical uncertainty. Note that we do not present uncertainties of matrix elements in Tab. VI; this is to avoid creating false impression that these specific matrix elements have been independently determined from the present Coulomb excitation data. Their uncertainties, used for example to calculate uncertainties of shape parameters in Sec. IV D, are calculated from the uncertainties of transition probabilities resulting from previous measurements.

The analysis yielded in particular two important quantities, determined for the first time: the $\langle 2_2^+ \| E2 \| 0_2^+ \rangle$ matrix element and the spectroscopic quadrupole moment of the 2_2^+ state. Their large values are consistent with a highly-deformed character of the side band in ^{42}Ca. Other matrix elements obtained in the present analysis

TABLE V. Reduced transitional and diagonal $E2$ matrix elements between the low-lying states in ^{42}Ca, and corresponding B($E2$) values and spectroscopic quadrupole moments determined in the course of the present analysis. Present experimental results are compared with previously measured values, SM and BMF calculations, as well as the OCM predictions [111].

$I_i^+ \rightarrow I_f^+$	$\langle I_i\|E2\|I_f\rangle$ [e·fm^2]			B($E2\downarrow; I_i^+ \rightarrow I_f^+$) [W.u.]				
	Present	SM	BMF	Present	Previous	SM	BMF	OCM [111]
$2_1^+ \rightarrow 0_1^+$	$20.5\,^{+0.6}_{-0.6}$	11.5	9.14	$9.7\,^{+0.6}_{-0.6}$	9.3 ± 1 [50]	3.05	1.9	5.6
					11 ± 2 [78]			
					9 ± 3 [81]			
					8.5 ± 1.9 [46]			
$4_1^+ \rightarrow 2_1^+$	$24.3\,^{+1.2}_{-1.2}$	11.3	12.2	$7.6\,^{+0.7}_{-0.7}$	50 ± 15 [78]	1.6	1.85	7.3
					11 ± 3 [81]			
					$10\,^{+10}_{-8}$ [46]			
$6_1^+ \rightarrow 4_1^+$	$9.3\,^{+0.2}_{-0.2}$	8.2	14.3	$0.77\,^{+0.03}_{-0.03}$	0.7 ± 0.3 [81]	0.6	1.8	1.95
$0_2^+ \rightarrow 2_1^+$	$22.2\,^{+1.1}_{-1.1}$	11.9	6.1	$57\,^{+6}_{-6}$	64 ± 4 [81]	16.3	4.3	3.5
					100 ± 6 [78]			
					55 ± 1 [75]			
					64 ± 4 [46]			
$2_2^+ \rightarrow 0_1^+$	$-6.4\,^{+0.3}_{-0.3}$	9.4	4.4	$1.0\,^{+0.1}_{-0.1}$	2.2 ± 0.6 [78]	2.04	0.5	0.35
					1.5 ± 0.5 [81]			
					1.2 ± 0.3 [46]			
$2_2^+ \rightarrow 2_1^+$	$-23.7\,^{+2.3}_{-2.7}$	-13.6	-7.7	$12.9\,^{+2.5}_{-2.5}$	17 ± 11 [78]	4.3	1.4	0.83
					$19\,^{+22}_{-14}$ [81]			
					$14\,^{+35}_{-9}$ [46]			
$4_2^+ \rightarrow 2_1^+$	$42\,^{+3}_{-4}$	21.9	10.1	$23\,^{+3}_{-4}$	30 ± 11 [78]	6.3	1.3	0.11
					16 ± 5 [81]			
					$12\,^{+7}_{-4}$ [46]			
$2_2^+ \rightarrow 0_2^+$	$26\,^{+5}_{-3}$	32	42	$15\,^{+6}_{-4}$	<61 [81]	24	40.7	37
					<46 [46]			
$4_2^+ \rightarrow 2_2^+$	$46\,^{+3}_{-6}$	52	70	$27\,^{+4}_{-6}$	60 ± 30 [81]	35	63	35.7
					60 ± 20 [78]			
					$40\,^{+40}_{-30}$ [46]			

	$\langle I_i\|E2\|I_i\rangle$ [e·fm^2]			Q_{sp} [e·fm^2]				
2_1^+	$-16\,^{+9}_{-3}$	-4.3	0.1	$-12\,^{+7}_{-2}$	-19 ± 8 [50]	-3	0.5	-14.3
2_2^+	$-55\,^{+15}_{-15}$	-31	-42	$-42\,^{+12}_{-12}$		-23	-32	

are, in general, in agreement with the results of earlier measurements, and in several cases the precision has been considerably improved, notably for transitions deexciting the 4_2^+ state.

The obtained set of reduced matrix elements reproduces all lifetimes presented in Table III within 1σ uncertainty, with the exception of the 2_2^+ state. The value obtained in the present analysis indicates a longer lifetime for this state (0.3 ps), which is still in agreement with the literature value within 3σ limit.

Almost all branching ratios presented in Table IV were reproduced within 1σ uncertainty, with only I($4_2^+ \rightarrow 2_2^+$) / I($4_2^+ \rightarrow 2_1^+$) reproduced within 2σ and I($4_1^+ \rightarrow 2_2^+$) / I($4_1^+ \rightarrow 2_1^+$) within 3σ limits. The latter are not consistent with measured excitation cross sections to populate the 4_1^+, 4_2^+ and 2_2^+ states, and, consequently, if the

measured branching ratios are imposed, the intensities of transitions depopulating these states cannot be reproduced and the total χ^2 value increases.

The obtained spectroscopic quadrupole moment of the 2_1^+ state was found in the agreement with the literature value within 1σ range. The experiment was not sensitive to $E2/M1$ mixing ratios, hence the previously measured values should be understood as strong constraints rather than data points to be fitted, and consequently they were reproduced very well in the analysis.

IV. DISCUSSION

The obtained experimental results are discussed in the context of microscopic calculations performed with both

TABLE VI. Reduced transitional $E2$ and $M1$ matrix elements between the low-lying states in ^{42}Ca, included in the present analysis, and corresponding B($E2$) and B($M1$) values. These matrix elements were not determined from the present data set, but influence the extraction of matrix elements listed in Tab. V. The values corresponding to the final solution of the GOSIA fit are compared with the results of previous measurements, SM and BMF calculations, as well as the OCM predictions [111].

	$\langle I_i\|E2\|I_f\rangle$ [e·fm^2]			B($E2\downarrow;I_i^+\to I_f^+$) [W.u.]				
$I_i^+ \to I_f^+$	Present	SM	BMF	Present	Previous	SM	BMF	OCM [111]
$6_1^+ \to 4_1^+$	9.3	8.2	14.3	0.72	0.72 ± 0.02 [72]	0.6	1.8	1.95
					0.74 ± 0.25 [81]			
					0.74 ± 0.03 [58]			
					0.77 ± 0.02 [79]			
$6_2^+ \to 4_2^+$	75	63	92	50	50 $^{+35}_{-16}$ [70]	35	75	35.2
$2_3^+ \to 0_1^+$	4.2	4.1	1	0.4	0.4±0.12 [81]	0.4	0.02	0.05
$2_3^+ \to 2_1^+$	18	11	5	7.5	7.5±2.3 [81]	2.8	0.6	0.10
$2_3^+ \to 0_2^+$	12	7	9	2.0	2.0±0.6 [81]	1.1	1.9	3.15
$2_3^+ \to 2_2^+$	20	24	31	9	9±9^a	13	22	
					~2.3 [81]			

	$\langle I_i\|M1\|I_f\rangle$ [μ_n]			B($M1\downarrow;I_i^+\to I_f^+$) [W.u.]				
$I_i^+ \to I_f^+$	Present	SM	BMF	Present	Previous	SM	BMF	
$2_2^+ \to 2_1^+$	0.97	0.78	-0.48	0.11	0.11±0.01 [65]	0.07	0.03	
$2_3^+ \to 2_1^+$	0.16	0.21	-0.04	0.0029	0.0029$^{+12}_{-7}$ [78]	0.005	0.0002	

^{a} calculated from the branching ratio reported in Ref. [46] and the lifetime of 2_3^+ state from Ref. [81].

shell model (SM) and beyond-mean-field model (BMF) approaches. Comparisons with other calculations for ^{42}Ca are also presented, as well as an attempt to discuss the measured $E2$ matrix elements using a phenomenological two-state mixing model and the quadrupole sum rule method.

A. Large-scale shell model calculations

In order to investigate the origins of the unexpected quadrupole collectivity, which has been observed in the magic nucleus ^{42}Ca, shell-model calculations were performed using the SDPF.MIX interaction in the $sdpf$ model space for neutrons and protons, with a virtual ^{28}Si core [92]. This interaction has proven successful in describing properties of the superdeformed bands in ^{40}Ca and ^{36}Ar and allows for the reproduction of the observed ground-state magnetic moments of ^{49,51}Ca and quadrupole moments of ^{47,49,51}Ca [93]. In spite of freezing of the excitations from the $1d_{5/2}$ orbit, and taking into account only excitations up to $8p-8h$, the diagonalization of the matrix of dimension $O(4.10^9)$, performed using the Antoine shell-model code [94, 95], was challenging. This level of truncation was verified to ensure convergence of the calculated spectroscopic properties in ^{42}Ca. The electric effective charges used in the calculation were $1.5e$ for protons and $0.5e$ for neutrons, whereas the effective gyromagnetic factors were $(g_\pi^s, g_\pi^l) = (5.5857, 1.0)$ for protons and $(g_\nu^s, g_\nu^l) = (-3.8263, 0.0)$ for neutrons.

The energies of excited states calculated within the shell model are in excellent agreement with the data, as shown in Fig. 11. The $E2$ matrix elements in the yrast band are underestimated, and those in the side band overestimated with respect to the present experimental results. That means that the mixing between the two bands is not fully reproduced, as discussed in detail in Sec. IV D. On the other hand, the experimental $M1$ transition strengths are quite well reproduced by the present calculation, as shown in Tab. VI.

The quadrupole properties of the lowest non-yrast 2^+ states (Tab. VII), calculated in the laboratory frame, reveal collective aspects:

- $Q_s(2_3^+, K = 2)$ is nearly equal to $Q_s(2_2^+, K = 0)$, and they have opposite signs,

- $Q_s(3_1^+, K = 2)$ is close to zero ($0.14e.fm^2$) and the low-lying 3_1^+ state is connected by a strong transition to the 2_3^+ state.

Furthermore, the intrinsic quadrupole moments Q_0 derived from calculated in-band $E2$ matrix elements via [96]:

$$\langle I_f, K\|E2\|I_i, K\rangle = \sqrt{2I_i + 1}(I_i, K, 2, 0|I_f, K)\sqrt{\frac{5}{16\pi}}eQ_0$$
(1)

or from the spectroscopic quadrupole moments via:

$$Q_0 = \frac{(J + 1)(2J + 3)}{3K^2 - J(J + 1)}Q_s(J)$$
(2)

are similar for the two excited bands, as presented in Tab. VIII.

These observations are consistent with a deformed character of excited states in ^{42}Ca and suggest that the structure built on 2_3^+ state is a $K = 2$ γ band, with the configuration dominated by almost equal contributions of $6p - 4h$ and $8p - 6h$ excitations ($\sim 40\%$ each). The difference between the Q_0 values obtained from the transitional and diagonal $E2$ matrix elements, presented in Tab. VIII, may be attributed to triaxiality.

TABLE VII. Quadrupole properties of the 2_2^+ and 2_3^+ states in ^{42}Ca, obtained in the present shell-model calculation.

J_i^+	2_2^+	2_3^+
Q_s [efm^2]	-23.2	18.5
B($E2, J_i^+ \to 0_i^+$) [e^2fm^4]	201.3	17.9
B($E2, 3^+ \to J_i^+$) [e^2fm^4]	26.1	371.6

TABLE VIII. Intrinsic quadrupole moments Q_0 of the $K = 0$ and $K = 2$ bands extracted from calculated spectroscopic quadrupole moments and B($E2$) transition strengths.

	Q_0 from Q_s [efm^2]	Q_0 from B(E2) [efm^2]
2_2^+	81	100
4_2^+	92	102
6_2^+	91	98
2_3^+	65	102
3_1^+	-	102

The quadrupole properties of the excited states calculated in the laboratory frame can be related to the nuclear shape in order to investigate the nature of observed structures, in particular that of the γ band. In Tab. IX we present the β and γ deformation parameters for the $0_{1,2}^+$ states in ^{42}Ca derived from the $E2$ matrix elements obtained in the present shell-model calculation using the Davydov-Filipov geometric model [97], Kumar and Cline's sum-rule approach [49, 115], and Constrained Hartree-Fock in the shell-model basis (CHFSM) [99, 100].

In the Davydov-Filipov model [97], the γ angle can be extracted from the ratio B($E2, 2_\gamma^+ \to 2^+$)/B($E2, 2_\gamma^+ \to 0^+$), and the β deformation parameter from the Q_0 intrinsic quadrupole moment, following:

$$Q_0 = \sqrt{\frac{16\pi}{5}} \frac{3}{4\pi} Ze R_0^2 \beta \qquad (3)$$

with $R_0 = 1.2 A^{1/3}$.

The CHFSM is a simple standard Hartree-Fock procedure restricted to the shell-model m-scheme configuration basis and used as a simplified alternative to exact diagonalizations [99, 100]. The Hartree-Fock equations are solved and constrained on the quadrupole degrees of

TABLE IX. β deformation parameter and the γ angle calculated using the Davydov-Filipov model, CHFSM, and Kumar-Cline sum rules, compared to the experimental values obtained from the sum rules (Tabs. XI,XII)

	0_1^+		0_2^+	
Davydov	0.09	12°	0.34	23°
CHFSM	0.03	60°	0.40	20°
sum rules	0.22	15°	0.46	18°
Exp	0.26(2)[a]	28(3)°	0.43(4)	$13(^{+5}_{-6})°$

[a] Deformation of the ground state is dynamic, as explained in detail in Sec. IV D, hence β and γ parameters presented here for 0_1^+ state can be understood as the mean values of the deformation.

freedom, to obtain the minimal energies as function of β and γ deformation parameters.

Finally, the quadrupole deformation parameters can be extracted using the $E2$ sum rules, proposed by Kumar [98], as detailed in Sec. IV D. It is worth noting that by using the strength function in the calculation of the sum rule we can get all the intermediate states reached from the initial states by $E2$ transitions. The values listed in Tab. IX result from the summation over all calculated intermediate states, unlike those in Tabs. XI,XII, where the sum was limited to states that were accessible experimentally.

As shown in Tab. IX, the deformation parameters obtained using the three methods are consistent for the 0_2^+ state, and they are in a good agreement with the experimental value. However, for the ground state we obtain β parameters close to zero using the Davydov-Filippov model and CHFSM (see Fig. 13a), while the sum rules yield a much larger value, closer to what is observed experimentally. This is related to the fact that the deformation of the 0_2^+ state has a static character, while the ground state exhibits large fluctuations about a spherical minimum, as discussed in Ref. [34].

B. Beyond mean field

In the present work we have performed BMF calculations within the symmetry conserving configuration mixing (SCCM) method [101] using the Gogny D1S interaction [102] to define the corresponding energy density functionals. This framework is very well suited to analyze the different states present in the low-lying spectra of atomic nuclei in terms of intrinsic shapes. In the SCCM method the nuclear states are obtained as linear combinations of particle number and angular momentum projected mean-field states. The coefficients of the linear combination are calculated self-consistently following the generator coordinate method (GCM) [103]. On the other hand, the mean-field states are found by solving the particle-number variation-after-projection (PN-

VAP) Hartree-Fock-Bogolyubov (HFB) equations with constraints in the quadrupole operators parametrized by (β_2, γ) [104].

The PN-VAP energy defined in the (β_2, γ) plane yields qualitative information on the quadrupole properties of the nucleus under study. In Fig. 9(a) such a potential energy surface (PES) is plotted for the ^{42}Ca isotope. This PES shows a very well-defined spherical minimum, consistent with the semi-magic character of this nucleus. In addition, a secondary minimum at $(\beta_2, \gamma) \approx (0.5, 20°)$ is found at a rather large excitation energy ($\sim$ 8 MeV). The specific shapes related to these minima (spherical and triaxially deformed) are better visualized if we represent the spatial densities that correspond to those HFB states (see inset in Fig. 9(a)).
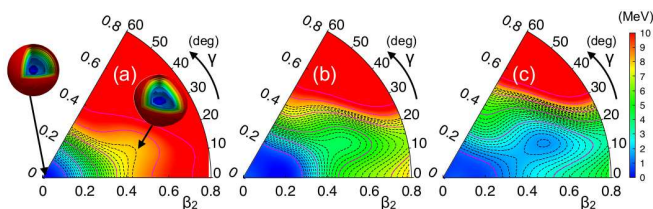

FIG. 9. (color online) Potential energy surfaces computed with the Gogny D1S interaction and: (a) Particle number variation-after-projection (PN-VAP); (b) particle number and angular momentum projection (PNAMP) with $J = 0$; and (c) PNAMP with $J = 2$. Energies in each plot are normalised to that in its minimum and contour lines are separated by 0.25 MeV (dashed lines) and 2 MeV (solid lines), respectively. Inset in (a): Spatial densities corresponding to each minimum found in PN-VAP calculations.

If we project the intrinsic HFB states onto particle numbers and angular momentum, we obtain the PES represented in Fig. 9(b)-(c) for $J = 0$ and $J = 2$. Now the degeneracy around the spherical shape is larger within the triangle defined by $(\beta_2, \gamma) = (0, 0°)$, $(0.25, 0°)$ and $(0.2, 60°)$ and the correlation energy gained by the symmetry restoration brings the energy of the deformed state closer to that of the spherical one.

The last step in the SCCM calculation is the shape mixing within the GCM framework [101]. As a result, we obtain the spectrum shown in Fig. 11 and the electromagnetic matrix elements in the laboratory frame used in Tabs. V-XIV. After this mixing the lowest excited states can be grouped into three bands built on top of the 0^+_1 ($\Delta J = 2$), 0^+_2 ($\Delta J = 2$) and 2^+_3 ($\Delta J = 1$) states, respectively. The ground-state band is characterized by small $E2$ transition probabilities and spectroscopic quadrupole moments, as expected for a spherical semi-magic configuration. In contrast, larger in-band transitions are predicted in the second and third bands. In order to investigate the underlying shapes of the states belonging to these bands we analyse the collective wave functions (c.w.f.) of the band heads, as presented in Fig. 10. The c.w.f. represent the weights of each (β_2, γ) deformation

in the nuclear states obtained within the SCCM framework. Hence, the most important contribution to the ground state comes from the spherical point and its surroundings (Fig. 10(a)). For the states belonging to the second band (0^+_2, 2^+_2, ...) the most relevant shapes are found around $(\beta_2, \gamma) = (0.55, 20°)$, consistent with the large electromagnetic transitions and negative spectroscopic quadrupole moments obtained in the present calculations. The third band shows rather similar c.w.f. to those in the second band, corroborating its character of a γ-band ($K = 2$) built on the second band. The comparison of obtained transition probabilities and quadrupole moments with both the experimental results and SM calculations shows a very good qualitative agreement.
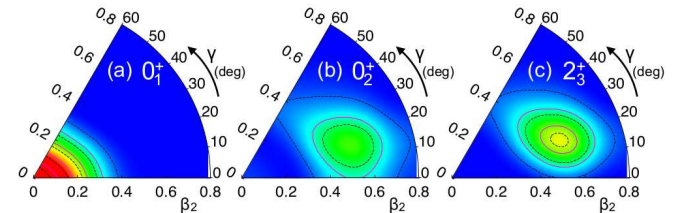

FIG. 10. (color online) Collective wave functions for the bandhead states obtained with BMF calculations with the Gogny D1S interaction. Red (blue) regions represent large (small) contributions to the wave functions.

The comparison between the experimental level scheme and those obtained from theoretical calculations is presented in Fig. 11. The shell-model calculations reproduce the level scheme of ^{42}Ca remarkably well, while all level energies are overestimated by BMF calculations, with the ground-state band being too stretched and the side band having a level spacing similar to what is observed experimentally, but appearing at a higher excitation energy. This can be explained by the lack of some degrees of freedom in the set of HFB wave functions used to perform the symmetry restoration and shape mixing. For example, the inclusion of cranking states allows for a better variational exploration of the states with $J \neq 0$ compressing the spectrum [106–108]. Moreover, energies of the excited 0^+ states can be affected by adding pairing fluctuations [105] and/or quasiparticle excitations explicitly [109]. Unfortunately, these improvements of the many-body method are very time consuming. We do not expect, however, that they would bring a change in the interpretation of the collective structure of this nucleus.

C. Two-state mixing model

The $\langle Q^2 \rangle$ quadrupole invariants experimentally determined for the $0^+_{1,2}$ and $2^+_{1,2}$ states in ^{42}Ca (Ref. [34], see also Sec. IV D of the present paper) remain constant within the side band, while for the ground state band an
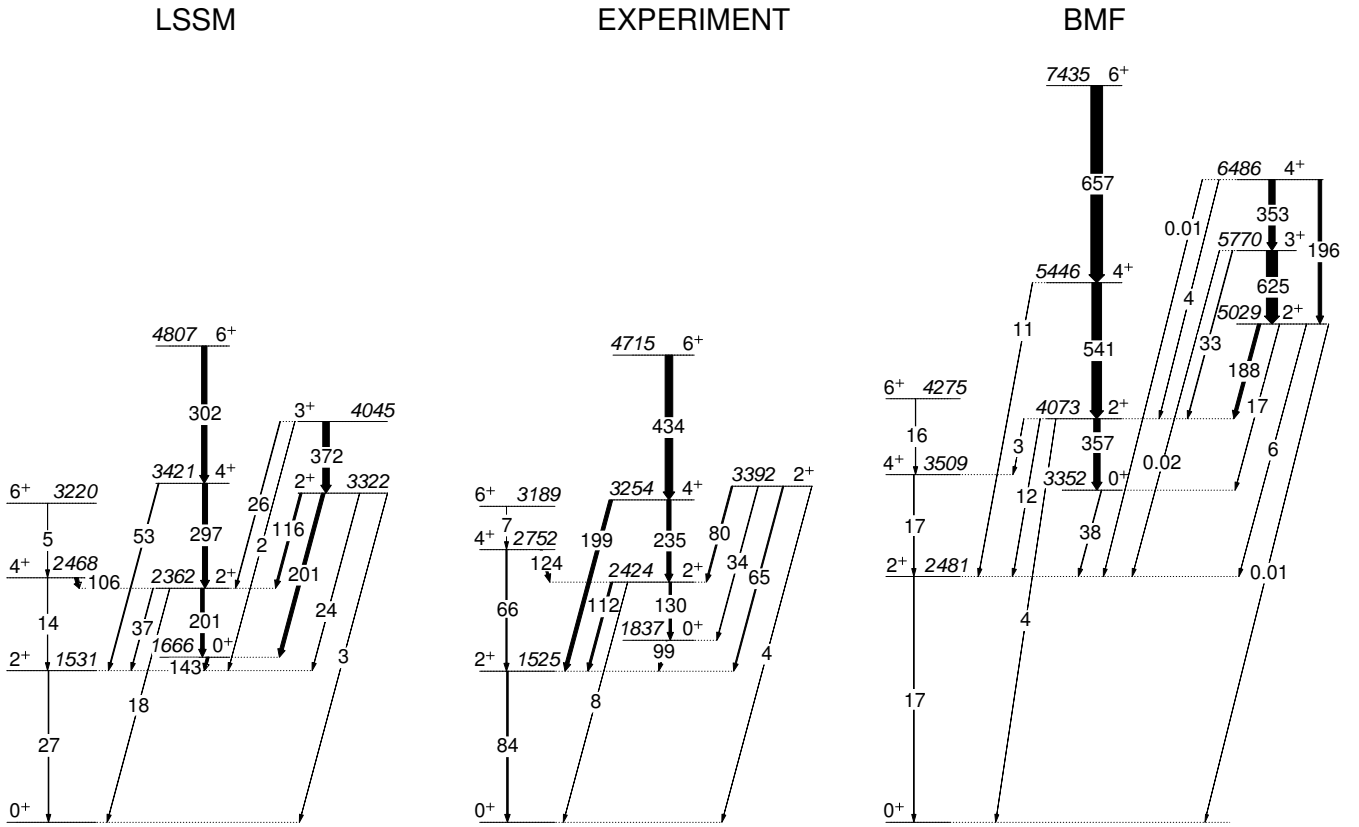
FIG. 11. Level schemes comparison: shell model (left), experiment (middle), beyond mean field (right). Level energies (in keV) are given in italic. The widths and labels of the arrows represent the measured and calculated B(E2,↓) values in $e^2 \text{fm}^2$.

important increase is observed between the 0_1^+ and the 2_1^+ states. This effect can be attributed to a possible mixing of the 2^+ states, consistent with one-neutron transfer reaction spectroscopy [66, 87], therefore we attempt to interpret the measured $E2$ matrix elements in the framework of a phenomenological two-state mixing model (see Ref. [88] and the references therein).

The model is based on the assumption that the observed physical states can be expressed as linear combinations of two pure structures. The mixing of states with the same spin-parity I^π is described by a mixing angle θ_I, which can be calculated using the set of experimental matrix elements. To calculate mixing angles between the lowest 0^+ and 2^+ states in ^{42}Ca, the equations listed in the Section V.A. of Ref. [88] were used, and the results are presented in Tab. X. The calculated mixing angle for the 0^+ states, $\cos^2(\theta_0)$=0.88(4), indicates that 0^+ states in ^{42}Ca are weakly mixed, and is consistent with the values obtained using theoretical matrix elements. The same quantity can be determined using the experimental value of the $\rho^2(E0; 0_2^+ \to 0_1^+)$ transition strength, provided that the deformation parameters are known. In a two-level mixing scenario the $E0$ strength is given by [90, 91]:

$$\rho^2(E0) = \left(\frac{3Z}{4\pi}\right)^2 \cos^2(\theta_0)\sin^2(\theta_0)$$
$$\cdot \left[\left(\beta_1^2 - \beta_2^2\right) + \frac{5\sqrt{5}}{21\sqrt{\pi}}\left(\beta_1^3\cos\gamma_1 - \beta_2^3\cos\gamma_2\right)\right]^2, \quad (4)$$

where $\sin(\theta_0)$ is the amplitude of the admixed wave function with shape parameters (β_1, γ_1) (in this case, the 0_2^+ state) in the lower lying level (the ground state) with (β_2, γ_2). The shape parameters for the 0_2^+ state are taken to be $\beta = 0.43(4)$, and $\gamma \approx 13(5)°$[34], whereas for the ground state the assumption is made that $\beta = 0$. In this case, Eq. 4 reduces to

$$\rho^2(E0) \approx \left(\frac{3Z}{4\pi}\right)^2 \cos^2(\theta_0)\sin^2(\theta_0)$$
$$\cdot \left[\beta_1^2 + \frac{5\sqrt{5}}{21\sqrt{\pi}}\beta_1^3\cos\gamma_1\right]^2. \quad (5)$$

Solving for $\cos^2(\theta_0)$ and using the experimental value of $1000 \cdot \rho^2(E0; 0_2^+ \to 0_1^+)$ of 135(12) [90] yields 84(4)%,

which is consistent with 88(4)% obtained in the analysis of the $E2$ matrix elements.

The obtained $\cos^2(\theta_2)$=0.39(8) value shows, however, that the simple two-level mixing model cannot be applied to the first two 2^+ states in ^{42}Ca, as this value suggests that the ground state has a 61% admixture of the deformed configuration, and vice versa. We suggest that this is related to the strong coupling of the 2_3^+ state to both 2_1^+ and 2_2^+: in both calculations the B(E2; $2_3^+ \rightarrow 2_2^+$) value is much larger than B(E2; $2_3^+ \rightarrow 2_1^+$), while the experimental transition strengths are similar. This would suggest that the mixing may involve all three 2^+ states, and, therefore, that the present model is too simple.

TABLE X. Mixing amplitudes for the 0^+ and 2^+ states in ^{42}Ca obtained from measured and calculated $E2$ matrix elements.

	Experiment	SM	BMF
$\cos^2(\theta_0)$	0.88(4)	0.85	0.96
$\cos^2(\theta_2)$	0.39(8)	0.83	0.97

The same model has been applied to our results in Ref. [89]. In addition to reaching similar conclusions on the mixing of the 0^+ and 2^+ states, the author obtained weak mixing ($\cos^2(\theta_4)$=0.94(17)) of the 4^+ states in ^{42}Ca. The consequences of changing the sign of the $\langle 0_1^+ \| E2 \| 2_2^+ \rangle$ matrix element were also explored: it leads to lower purity of the 0^+ states ($\cos^2(\theta_0)$=0.75(3)) and slightly weaker mixing of the 2^+ states ($\cos^2(\theta_2)$=0.43(3)), again showing that the two-state model is not applicable in this case.

For comparison, we can apply the two-state mixing model to matrix elements obtained from theoretical calculations. The results, presented in Tab. X, show that the two structures predicted by both theories mix weakly independent of the spin.

D. Quadrupole deformation parameters

The Quadrupole Sum Rules method [49, 115, 116] can be applied to the obtained $E2$ matrix elements in order to extract information on the charge distribution of the nucleus in specific states. The results were published in Ref. [34]; here we would like to present the method in more detail, and analyse the contributions of individual matrix elements to the resulting invariants.

The Quadrupole Sum Rules method is based on the fact that the electric multipole transition operator E(λ=2, μ) is a spherical tensor and it can be represented using two parameters: Q, the overall quadrupole deformation parameter equivalent to the elongation parameter β in Bohr's model, and δ, which is related to the triaxiality parameter γ.

The expectation values of the quadrupole rotational invariants $\langle Q^2 \rangle$ and $\langle Q^3 \cos(3\delta) \rangle$ which describe the deformation of individual states in both the intrinsic and laboratory frames are determined using the set of $E2$ matrix elements by an expansion over all possible intermediate states using Wigner's $6j$ symbols:

$$\frac{1}{\sqrt{5}} \langle Q^2 \rangle = \langle I_i \| [E2 \times E2]_0 \| I_i \rangle$$

$$= \frac{1}{\sqrt{2I_i + 1}} \sum_j \langle I_i \| E2 \| I_j \rangle \langle I_j \| E2 \| I_i \rangle \begin{Bmatrix} 2 & 2 & 0 \\ I_i & I_i & I_j \end{Bmatrix}, \quad (6)$$

$$\langle Q^3 \cos(3\delta) \rangle = \langle I_i \| \{ [E2 \times E2]_2 \times E2 \}_0 \| I_i \rangle$$

$$= \mp \frac{\sqrt{35}}{\sqrt{2}} \frac{1}{\sqrt{2I_i + 1}} \cdot$$

$$\cdot \sum_{jk} \langle I_i \| E2 \| I_j \rangle \langle I_j \| E2 \| I_k \rangle \langle I_k \| E2 \| I_i \rangle \begin{Bmatrix} 2 & 2 & 2 \\ I_i & I_j & I_k \end{Bmatrix}. \quad (7)$$

The first of the presented invariants is a measure of overall quadrupole deformation and is proportional to the sum of squared $E2$ matrix elements $\langle i \| E2 \| t \rangle \langle t \| E2 \| i \rangle$ over all intermediate states $|t\rangle$ that can be reached from the state in question $|i\rangle$ in a single $E2$ transition. The higher-order invariant $\langle Q^3 \cos(3\delta) \rangle$ that provides information on triaxial symmetry, is constructed of triple products of $E2$ matrix elements ($\langle i \| E2 \| t \rangle \langle t \| E2 \| u \rangle \langle u \| E2 \| i \rangle$, where $|i\rangle$ – initial state, $|t\rangle$ and $|u\rangle$ – intermediate states) and thus relative signs of $E2$ matrix elements entering the sum must be known.

The $\langle Q^2 \rangle$ values were obtained for the 0^+ and 2^+ states in both bands, as presented in Table XII and in Fig. 12. Since the present measurement yielded relative signs of $E2$ matrix elements coupling the 0^+ and 2^+ states, it was also possible to determine the $\langle Q^3 \cos(3\delta) \rangle$ invariants for the 0_1^+ and 0_2^+ states (Table XI and XII), as in Refs. [117, 118].

TABLE XI. Experimental and theoretical quadrupole invariants, $\langle Q^2 \rangle$ [e^{2}fm^4] and $\sigma(Q^2)$ [e^{2}fm^4], for the $0_{1,2}^+$ and $2_{1,2}^+$ states in ^{42}Ca. Variances $\sigma(Q^2)$ are calculated from $\langle Q^4(0) \rangle$ listed in Tab. XII.

state	EXP		SM		BMF	
	$\langle Q^2 \rangle$	$\sigma(Q^2)$	$\langle Q^2 \rangle$	$\sigma(Q^2)$	$\langle Q^2 \rangle$	$\sigma(Q^2)$
0_1^+	500 (20)	350 (30)	240	470	100	250
2_1^+	900 (100)		250	490	100	310
0_2^+	1300 (230)	350 (30)	1200	500	1900	520
2_2^+	1400 (250)		1130	500	1900	300

In order to compare the deformation of each individual state with the theoretical results, the Quadrupole Sum Rule method was applied to matrix elements resulting from theoretical calculations in the same way as it was done for the experimental ones. As described in Ref. [34],

TABLE XII. Experimental and theoretical $\langle Q^4 \rangle$ invariants [$\cdot 10^4$ e^{4}fm^8] and $\langle \cos(3\delta) \rangle$ values, calculated from $\langle Q^3 \cos(3\delta) \rangle$ as in Ref. [117, 118].

		$\langle Q^4(0) \rangle$	$\langle Q^4(2) \rangle$	$\langle Q^4(4) \rangle$
0_1^+	EXP	35(6)		
	SM	30	30	20
	BMF	10	10	10
0_2^+	EXP	185(13)		
	SM	170	160	140
	BMF	390	380	380

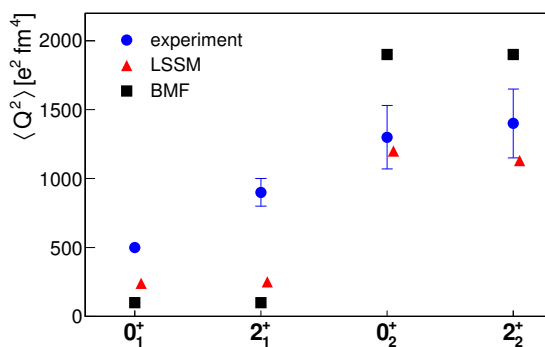|	$\langle \cos(3\delta) \rangle_{exp}$	$\langle \cos(3\delta) \rangle_{SM}$	$\langle \cos(3\delta) \rangle_{BMF}$
0_1^+	0.06 (10)	0.34	0.34
0_2^+	0.79 (13)	0.67	0.49

FIG. 12. (Color online) Experimental and theoretical $\langle Q^2 \rangle$ invariants for the $0_{1,2}^+$ and $2_{1,2}^+$ states in ^{42}Ca.

the non-zero $\langle Q^2 \rangle$ value obtained for the 0_1^+ state corresponds to fluctuations about a spherical shape. This is consistent with the maximum triaxiality obtained for this state, which results from averaging over all possible deformed shapes. The confirmation of this interpretation comes from the fact that the magnitude of dispersion of $\langle Q^2 \rangle$, defined as $\sigma(Q^2) = \sqrt{\langle Q^4 \rangle - \langle Q^2 \rangle^2}$ [119] is comparable to $\langle Q^2 \rangle$, as presented in Tab. XII. The $\langle Q^4 \rangle$ shape invariant is given by the fourth-order product:

$$P^4(J) = \langle I_i \| \{ (E2 \times E2)^J \times (E2 \times E2)^J \}^0 \| I_i \rangle$$
$$= \sum_{jkl} \frac{(2J+1)^{1/2}}{\sqrt{2I_i+1}} \cdot (-1)^{I_i - I_j}$$
$$\cdot \langle I_i \| E2 \| I_j \rangle \langle I_j \| E2 \| I_k \rangle \langle I_k \| E2 \| I_l \rangle \langle I_l \| E2 \| I_i \rangle \cdot$$
$$\cdot \begin{Bmatrix} 2 & 2 & J \\ I_i & I_j & I_k \end{Bmatrix} \begin{Bmatrix} 2 & 2 & J \\ I_i & I_j & I_l \end{Bmatrix} \quad (8)$$

with $J = 0, 2, 4$ being the spin that a pair of $E2$ operators is coupled to.

The three independent estimates of $\langle Q^4 \rangle$ can be evaluated using $P^4(J)$ for $J = 0, 2, 4$, via:

$$\langle Q^4(0) \rangle = 5 P^4(0), \quad (9)$$

$$\langle Q^4(2) \rangle = \frac{7\sqrt{5}}{2} P^4(2), \quad (10)$$

$$\langle Q^4(4) \rangle = \frac{35}{6} P^4(4). \quad (11)$$

The values of $\langle Q^4(4) \rangle$ obtained using the three possible intermediate spins J should be the same, which proves the consistency of the set of matrix elements and its completeness. The currently known set of experimentally obtained matrix elements, although rich, is only sufficient to obtain the expectation value of $\langle Q^4(0) \rangle$. The $\langle Q^4(0) \rangle$, $\langle Q^4(2) \rangle$ and $\langle Q^4(4) \rangle$ values obtained from sets of matrix elements resulting from BMF calculations are very similar for each of the two states, while the $\langle Q^4(4) \rangle$ obtained from LSSM calculations isalways lower than the other two: this is related to the fact that no matrix elements involving the 4_3^+ state were calculated within this approach.

The behaviour of $\langle Q^2 \rangle$ and its dispersion is remarkably consistent for both theoretical approaches, as shown in Fig. 12 and in Tab. XII. For the ground-state band, $\sigma(Q^2)_{SM}$ and $\sigma(Q^2)_{BMF}$ values are comparable with $\langle Q^2 \rangle$, as one would expect for fluctuations about a spherical minimum of potential. For the side band, however, the dispersion is much lower than the actual value, which is interpreted as a static deformation.

It should be noted that the deformation predicted by both theoretical approaches remains constant within each band. This is confirmed by the experimental results for the highly-deformed structure, but those for the ground-state band show that the $\langle Q^2 \rangle$ for the 2_1^+ state is considerably larger than the value obtained for the ground state. This is consistent with the large mixing of the 2^+ states as discussed in Sec. IV C, suggesting that the 2_1^+ has a considerable admixture of the well-deformed 2_2^+ and 2_3^+ states.

The contributions of individual matrix elements to the $\langle Q^2 \rangle$ invariants for the $0_{1,2}^+$ and $2_{1,2}^+$ states in ^{42}Ca is presented in Table XIII, both for experimental and theoretical values.

In almost all cases, the same matrix elements bring the most important contribution to the invariants calculated using experimental and theoretical matrix elements. The $\langle Q^2 \rangle$ for the ground state is dominated, as always, by the coupling to the 2_1^+ state, although its contribution to the experimental value is much larger than for those resulting from the calculations, especially using the SM (90% vs 55%). Different behaviour is observed for the 0_2^+ state, where again the dominant contribution comes from the in-band matrix element, but the influence of

matrix elements involving other 2^+ states is much larger for the experimental value, where they amount to 50% of the total, than for the theoretical calculations (16% and 6% for SM and BMF, respectively). This effect can be attributed to the mixing of 2^+ states being much larger in the experiment than in the theory. It should also be noted that the transition to the 2_3^+ state, although not observed in the present experiment. contributes to over 10% of the total $\langle Q^2 \rangle$ value for the 0_2^+ state.

For the 2_1^+ state, the dominant contribution to the invariant comes from an intra-band transitional matrix element $\langle 2_1^+ \| E2 \| 4_2^+ \rangle$, amounting to about 40% of the total for both experimental and SM values. For the 2_2^+ state, the value of the spectroscopic quadrupole moment of this state has the largest influence on the experimental value, while it is the $\langle 4_2^+ \| E2 \| 2_2^+ \rangle$ in-band matrix element that contributes almost 50% of the total for both theoretical calculations; this difference is due to the more triaxial shape of the superdeformed band in the calculations than in the experiment, related to the reduction of the static quadrupole moments in this structure.

Additionally, we have evaluated the possible contribution of higher-lying states in the γ band to the $\langle Q^2 \rangle$ invariants using the matrix elements obtained from the BMF calculation. As shown in Tab. XIII, the contributions of the loops involving the 3_1^+ and 4_3^+ states bring less than 3% to the total $\langle Q^2 \rangle$ values, and therefore we expect the systematic error related to non-completeness of the sum over intermediate states to be lower than the statistical error on the invariant.

For the $\langle Q^3 \cos(3\delta) \rangle$ invariant (see Tab.XIV), again there is a similarity between the calculations using experimental and theoretical matrix elements, with the dominant contributions coming from the same $E2 \times E2 \times E2$ loops, especially for the 0_2^+ state. For the 0_1^+ state, all $E2 \times E2 \times E2$ loops have similar influence on the final value of the invariant, and their contributions partly cancel out due to opposite signs. This is especially true for the invariant deduced from experimentally measured matrix elements. Here, in particular, we would like to note that the approximate formula proposed by Andrejtscheff and Petkov [120] to derive the $\langle Q^3 \cos(3\delta) \rangle$ invariant using only the first two $E2 \times E2 \times E2$ loops, works very well in the case of ^{42}Ca (600 $e^3 fm^6$ from the approximate calculation versus 800 $e^3 fm^6$ from the full sum rules formalism, which translates into γ angles of 29.1° and 28.9°, respectively). The most notable difference concerns the $E2 \times E2 \times E2$ loops involving the spectroscopic quadrupole moment of the 2_1^+ state, which is the main contribution to the $\langle Q^3 \cos(3\delta) \rangle$ for the 0_2^+ state obtained from the experimental results, and is much less important for those resulting from the theoretical calculations. This is due to the fact that this matrix element is strongly underestimated by theory. The only difference regarding the sign is observed for two $E2 \times E2 \times E2$ loops involving the $\langle 2_2^+ \| E2 \| 0_1^+ \rangle$ matrix element, being the only matrix element, which experimentally measured sign has not

TABLE XIII. Contribution of individual matrix elements to the values of the $\langle Q^2 \rangle$ shape invariants for 0_1^+, 2_1^+, 0_2^+ and 2_2^+ states in ^{42}Ca: experiment, SM and BMF.

State	Component $E2 \times E2$	Contribution to $\langle Q^2 \rangle$ [$e^2 fm^4$] Experiment	SM	BMF
0_1^+	$\langle 0_1^+ \| E2 \| 2_1^+ \rangle \langle 2_1^+ \| E2 \| 0_1^+ \rangle$	440	134	80
	$\langle 0_1^+ \| E2 \| 2_2^+ \rangle \langle 2_2^+ \| E2 \| 0_1^+ \rangle$	41	89	19
	$\langle 0_1^+ \| E2 \| 2_3^+ \rangle \langle 2_3^+ \| E2 \| 0_1^+ \rangle$	19	17	1
	$\langle Q^2 \rangle =$	500(20)	240	100
2_1^+	$\langle 2_1^+ \| E2 \| 0_1^+ \rangle \langle 0_1^+ \| E2 \| 2_1^+ \rangle$	85	28	18
	$\langle 2_1^+ \| E2 \| 0_2^+ \rangle \langle 0_2^+ \| E2 \| 2_1^+ \rangle$	100	30	8
	$\langle 2_1^+ \| E2 \| 2_2^+ \rangle \langle 2_2^+ \| E2 \| 2_1^+ \rangle$	113	38	13
	$\langle 2_1^+ \| E2 \| 4_1^+ \rangle \langle 4_1^+ \| E2 \| 2_1^+ \rangle$	120	27	32
	$\langle 2_1^+ \| E2 \| 4_2^+ \rangle \langle 4_2^+ \| E2 \| 2_1^+ \rangle$	362	99	22
	$\langle 2_1^+ \| E2 \| 2_3^+ \rangle \langle 2_3^+ \| E2 \| 2_1^+ \rangle$	66	25	6
	$\langle 2_1^+ \| E2 \| 2_1^+ \rangle \langle 2_1^+ \| E2 \| 2_1^+ \rangle$	54	4	0
	$\langle 2_1^+ \| E2 \| 4_3^+ \rangle \langle 4_3^+ \| E2 \| 2_1^+ \rangle$			0.4
	$\langle 2_1^+ \| E2 \| 3_1^+ \rangle \langle 3_1^+ \| E2 \| 2_1^+ \rangle$			-0.6
	$\langle Q^2 \rangle =$	900(100)	250	100
0_2^+	$\langle 0_2^+ \| E2 \| 2_1^+ \rangle \langle 2_1^+ \| E2 \| 0_2^+ \rangle$	488	142	37
	$\langle 0_2^+ \| E2 \| 2_2^+ \rangle \langle 2_2^+ \| E2 \| 0_2^+ \rangle$	645	1005	1776
	$\langle 0_2^+ \| E2 \| 2_3^+ \rangle \langle 2_3^+ \| E2 \| 0_2^+ \rangle$	168	52	86
	$\langle Q^2 \rangle =$	1300(230)	1200	1900
2_2^+	$\langle 2_2^+ \| E2 \| 0_1^+ \rangle \langle 0_1^+ \| E2 \| 2_2^+ \rangle$	8	18	4
	$\langle 2_2^+ \| E2 \| 2_1^+ \rangle \langle 2_1^+ \| E2 \| 2_2^+ \rangle$	109	38	12
	$\langle 2_2^+ \| E2 \| 4_1^+ \rangle \langle 4_1^+ \| E2 \| 2_2^+ \rangle$	62	3	3
	$\langle 2_2^+ \| E2 \| 0_2^+ \rangle \langle 0_2^+ \| E2 \| 2_2^+ \rangle$	126	207	360
	$\langle 2_2^+ \| E2 \| 4_2^+ \rangle \langle 4_2^+ \| E2 \| 2_2^+ \rangle$	411	551	980
	$\langle 2_2^+ \| E2 \| 2_3^+ \rangle \langle 2_3^+ \| E2 \| 2_2^+ \rangle$	92	119	190
	$\langle 2_2^+ \| E2 \| 2_2^+ \rangle \langle 2_2^+ \| E2 \| 2_2^+ \rangle$	592	193	351
	$\langle 2_1^+ \| E2 \| 4_3^+ \rangle \langle 4_3^+ \| E2 \| 2_1^+ \rangle$			5
	$\langle 2_1^+ \| E2 \| 3_1^+ \rangle \langle 3_1^+ \| E2 \| 2_1^+ \rangle$			-46
	$\langle Q^2 \rangle =$	1400(250)	1130	1900

been reproduced by the theory (see Tab.V).

For the 0_2^+ state, the main contributions to the $\langle Q^3 \cos(3\delta) \rangle$ invariant come from the $E2 \times E2 \times E2$ loops involving the $\langle 2_2^+ \| E2 \| 0_2^+ \rangle$ matrix element, as expected for a band head of a highly-deformed structure, which is consistent both with theoretical calculations and experimental results. It should be noted that the contribution of this single loop is close to the value of the entire $\langle Q^3 \cos(3\delta) \rangle$ invariant, with all other contributions cancelling out to some extent; this is especially true for the invariants calculated using experimental values of $E2$ matrix elements, and those resulting from LSSM calculations.

The $E2 \times E2 \times E2$ loops involving the $\langle 2_2^+ \| E2 \| 2_1^+ \rangle$ and $\langle 2_3^+ \| E2 \| 2_1^+ \rangle$ matrix elements are more important for the calculations using experimental values of matrix elements than for those obtained from the theory. This is related to the mixing of 2^+ states being underestimated by the theory.

The spectroscopic quadrupole moment of the 2_3^+ state has not been measured experimentally, hence in the present analysis it was assumed to be equal to zero.

TABLE XIV. Contribution of individual matrix elements to the values of the $\langle 0_1^+|Q^3\cos(3\delta)|0_1^+\rangle$ and $\langle 0_2^+|Q^3\cos(3\delta)|0_2^+\rangle$ shape invariants in ^{42}Ca: experiment, SM and BMF.

State	Component $E2\times E2\times E2$	Contribution to $\langle Q^3\cos(3\delta)\rangle$ [e³fm⁶]		
		Experiment	SM	BMF
0_1^+	$\langle 0_1^+\|E2\|2_1^+\rangle\langle 2_1^+\|E2\|2_1^+\rangle\langle 2_1^+\|E2\|0_1^+\rangle$	5800	500	0
	$\langle 0_1^+\|E2\|2_1^+\rangle\langle 2_1^+\|E2\|2_2^+\rangle\langle 2_2^+\|E2\|0_1^+\rangle$	-5200	2500	500
	$\langle 0_1^+\|E2\|2_1^+\rangle\langle 2_1^+\|E2\|2_3^+\rangle\langle 2_3^+\|E2\|0_1^+\rangle$	-2700	-900	-100
	$\langle 0_1^+\|E2\|2_2^+\rangle\langle 2_2^+\|E2\|2_2^+\rangle\langle 2_2^+\|E2\|0_1^+\rangle$	1900	2200	700
	$\langle 0_1^+\|E2\|2_2^+\rangle\langle 2_2^+\|E2\|2_3^+\rangle\langle 2_3^+\|E2\|0_1^+\rangle$	1000	-1600	-200
	$\langle 0_1^+\|E2\|2_3^+\rangle\langle 2_3^+\|E2\|2_3^+\rangle\langle 2_3^+\|E2\|0_1^+\rangle$	0	-300	0
	Sum of all contributions $\langle 0_1^+\|Q^3\cos(3\delta)\|0_1^+\rangle$	800	2400	900
	$\langle\cos(3\delta)\rangle$	0.06 (10)	0.34	0.34
0_2^+	$\langle 0_2^+\|E2\|2_1^+\rangle\langle 2_1^+\|E2\|2_1^+\rangle\langle 2_1^+\|E2\|0_2^+\rangle$	6800	500	0
	$\langle 0_2^+\|E2\|2_1^+\rangle\langle 2_1^+\|E2\|2_2^+\rangle\langle 2_2^+\|E2\|0_2^+\rangle$	22400	8600	3400
	$\langle 0_2^+\|E2\|2_1^+\rangle\langle 2_1^+\|E2\|2_3^+\rangle\langle 2_3^+\|E2\|0_2^+\rangle$	-8700	-1600	-500
	$\langle 0_2^+\|E2\|2_2^+\rangle\langle 2_2^+\|E2\|2_2^+\rangle\langle 2_2^+\|E2\|0_2^+\rangle$	30100	25800	62500
	$\langle 0_2^+\|E2\|2_2^+\rangle\langle 2_2^+\|E2\|2_3^+\rangle\langle 2_3^+\|E2\|0_2^+\rangle$	-12100	-9200	-20200
	$\langle 0_2^+\|E2\|2_3^+\rangle\langle 2_3^+\|E2\|2_3^+\rangle\langle 2_3^+\|E2\|0_2^+\rangle$	0	-1100	-3000
	Sum of all contributions $\langle 0_2^+\|Q^3\cos(3\delta)\|0_2^+\rangle$	38500	23000	42200
	$\langle\cos(3\delta)\rangle$	0.79 (13)	0.67	0.49

However, the contribution to the $\langle Q^3\cos(3\delta)\rangle$ invariant involving the corresponding matrix element is strongly suppressed independent of the $\langle 2_3^+\|E2\|2_3^+\rangle$ value, since it enters the sums multiplied by the $\langle 2_3^+\|E2\|0_1^+\rangle$ matrix element squared (or the $\langle 2_3^+\|E2\|0_2^+\rangle$ squared for the 0_2^+ state), which are small. This is confirmed by the theoretical calculations, that predict it to be on the level of 5-10% of the strongest contribution to $\langle Q^3\cos(3\delta)\rangle$ for both the 0_1^+ and 0_2^+ states.

The relative signs of all matrix elements involving the 2_3^+ state were adopted from the theory, thus the signs of the corresponding $E2\times E2\times E2$ loops are the same for the invariants obtained using experimental and theoretical values of matrix elements. A different combination of signs would have a minor influence on the $\langle Q^3\cos(3\delta)\rangle$ invariant for the 0_1^+ state, which would still correspond to a shape close to maximally triaxial. For the 0_2^+ state, changing the signs of the $E2\times E2\times E2$ loops involving the 2_3^+ state would lead to an increase of the $\langle Q^3\cos(3\delta)\rangle$ value closer to what would be expected for an axially symmetric nucleus, or even to non-physical solutions of $\cos(3\delta) > 1$. Measurement of the signs of matrix elements involving the 2_3^+ state remains a challenge for future Coulomb excitation experiments.

The $\langle Q^2\rangle$ and $\langle Q^3\cos(3\delta)\rangle$ invariants can be further converted to the β and γ collective model deformation parameters, as explained in detail in Ref.[116]. The $\beta=0.43(4)$ and $\gamma=13(^{+5}_{-6})^\circ$ deformation parameters obtained in this way for 0_2^+, show that the side band in ^{42}Ca has a slightly triaxial superdeformed shape, and can be directly compared to model predictions. Very good overall agreement is found: both potential energy sur-

face maps presented in Fig. 13, in addition to a spherical minimum for the ground-state band show a triaxial minimum that is located at $\beta_2=0.4$ and $\gamma \approx 20^\circ$ for CHFSM (panel (a)) and at $\beta_2=0.5$, $\gamma = 15^\circ$ for BMF calculations (panel (b)).
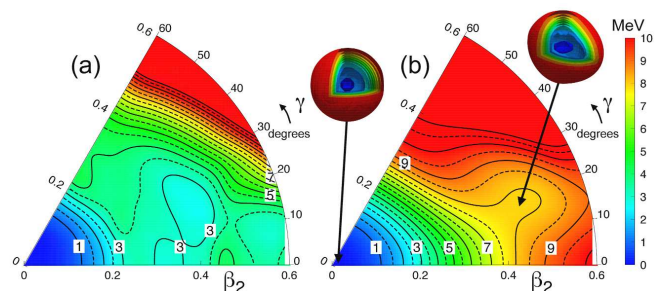

FIG. 13. (Color online) Potential energy surfaces resulting from deformation-constrained Hartree-Fock calculations with (a) SM interaction, and (b) BMF, particle number projection method (PN-VAP), Gogny D1S interaction. Spatial densities corresponding to each minimum found in BMF calculations are also shown in the panel (b). Reproduced from Ref. [34]

E. Other theoretical approaches

The structure of ^{42}Ca was also studied in the framework of the generator coordinate method (GCM) with deformed-basis antisymmetrized molecular dynamics (AMD) wave functions [110], the $\alpha+^{38}$Ar orthogonality condition model (OCM) [111] and covariant relativistic energy density functional theory (CDFT) [114].

In the AMD-GCM approach [110] Gogny D1S force was used as the effective interaction and the basis wave functions of the GCM were obtained via the energy variation with two types of constraints: the quadrupole deformation parameter of the total system, β, and the distance between the α and ^{38}Ar clusters. As a result, a rotational band of a predominantly $6p - 4h$ configuration and β deformation of about 0.4 was found with a band head at about 4 MeV excitation energy. By comparing the calculated intraband transition strengths with the experimental values, the authors identify this theoretical structure with the band built on the 0_2^+ state at 1837 keV. This is further supported by the the fact that the 0_2^+ state is weakly populated in α transfer, consistent with the obtained low admixture of the α-^{38}Ar cluster structure component. The obtained values of B($E2$; $2_2^+ \rightarrow 0_2^+$) = 28.5 W.u. and B($E2$; $4_2^+ \rightarrow 2_2^+$) = 33.1 W.u are in a very good agreement with our present experimental findings [34]. In addition, the calculations predicted a K=2 side band of the structure built on the 0_2^+ state, resulting from its triaxial deformation. On the other hand, the AMD calculations did not succeed in reproducing the level energies in ^{42}Ca, with the ground-state band built on $2p$ configuration being extremely compressed, and the side band appearing at the energy twice as high as observed experimentally.

Another type of α-cluster model was applied to ^{42}Ca in Ref. [111]. The OCM theoretical calculations describe the cluster and shell-model states in a unified way. The ground-state band in ^{42}Ca is found to have a two-particle nature, while the side band constructed on the 0_2^+ state has a predominantly $\alpha + ^{38}$Ar cluster structure. The 2_3^+ state is interpreted as resulting from coupling of an α cluster to the 2^+ state in ^{38}Ar. The calculated B($E2$) values are presented in Tab V. The in-band transition strengths, both in the ground-state and the side bands, are rather well reproduced, while the interband transitions are strongly overestimated. The calculated spectroscopic quadrupole moment of the 2_1^+ state is in good agreement with the experimental result, and its large negative value results mostly from the admixture of cluster components to the predominantly $2p$ 2_1^+ state. The $0_2^+ \rightarrow 0_1^+$ E0 transition strength was also reasonably well reproduced. The authors note that intra-band transition rates are very sensitive to small admixtures of $2p$ and α-cluster wave functions to the dominant configuration, and the model should not be expected to give more than a qualitative prediction of these properties.

Highly-deformed structures in ^{42}Ca were also studied in the framework of the cranked relativistic mean field theory (CRMF) [114]. The model does not assume the existence of cluster structures: the formation of cluster structures proceeds from microscopic single-nucleon degrees of freedom via many-body correlations. The side band based on the 0_2^+ state in ^{42}Ca seems to correspond to the [4,3] a configuration in Ref. [114], predicted to appear at about 1 MeV excitation energy and to have a

transitional quadrupole moment, Q_t, of about 1.5 eb (as compared to the experimental value of 1.13(10) eb). Triaxial deformation of $\gamma \sim -20°$ is expected for this structure, and the same is true for more deformed states in ^{42}Ca. Unfortunately, the predictions of this model do not include properties of the decay from the deformed structure to the yrast band.

V. SUMMARY

A Coulomb excitation experiment to study electromagnetic properties of ^{42}Ca was performed at INFN Laboratori Nazionali di Legnaro. For the first time, the superdeformation and triaxility of states in the side band in A~ 40 mass region was experimentally verified in a dedicated high-precision measurement. The phenomenological two band-mixing model gives further insight into the mixing of the wave functions, indicating a low degree of mixing between the 0^+ states and a significant one between the 2^+ states, but it is clearly too simple to describe all experimental data. A consistent description of the shape coexistence of a spherical ground state, exhibiting large fluctuations in the β-γ plane, and a rigid superdeformed side band in ^{42}Ca could be achieved by performing sophisticated state-of-the-art theoretical calculations in the framework of the large scale shell model and beyond mean-field approach. Expectation values of the quadrupole invariants of the 0^+ and 2^+ states in the ground-state and side bands in ^{42}Ca, related to the shape parameters, were derived in a model-independent way using the Quadrupole Sum Rules formalism, and the application of this method to the theoretical results helps to understand the complex structure of ^{42}Ca.

[1] H. A. Jahn and E. Teller, *Proc. Roy. Soc.* **A161**, 220 (1937).
[2] S.M. Polikhanov *et al.*, *Sov. Phys. JETP* **15**, 1016 (1962).
[3] H.J. Specht, J. Weber, E. Konecny and D. Heunemann, Phys. Lett. B 41, 43 (1972).
[4] V. Metag, D. Habs and H.J. Specht, Phys. Rep. 65, 1 (1980).
[5] P.J. Twin *et al.*, *Phys. Rev. Lett.* **57**, 811 (1986).
[6] P.J. Nolan *et al.*, *J. Phys.* **G 11**, L17 (1985).
[7] E. M. Beck *et al.*, *Phys. Rev. Lett.* **5**, 2182 (1987).
[8] E.F. Moore *et al.*, *Phys. Rev. Lett.* **63**, 360 (1989).
[9] T.L. Khoo *et al.*, *Phys. Rev. Lett.* **76**, 1583 (1996).
[10] A. Lopez-Martens *et al.*, *Phys. Lett.* **B380**, 18 (1996).
[11] R.B. Firestone, B. Singh and S.Y.F. Chu, Nuclear Data Sheets 97, 241, (2002).
[12] S. Raman, C.W Nestor and P. Tikkanen, *At. Data Nucl. Data Tables* **78**, 1 (2001).
[13] P. Fallon, *Nucl. Phys.* **A 752**, 231c (2005).
[14] E. Ideguchi *et al.*, *Phys. Rev. Lett.* **87**, 222501 (2001).
[15] C.J.Chiara *et al..*, Phys. Rev. C 67 041303(R) (2003)
[16] C.E. Svensson *et al.*, *Phys. Rev. Lett.* **85**, 2693 (2000).
[17] C.E. Svensson *et al.*, *Phys. Rev.* **C63**, 061301 (R) (2001).
[18] D. Rudolph *et al.*, *Phys. Rev.* **C65**, 034305 (2002).
[19] R.A.E. Austin, "Lifetimes of Superdeformed States in ^{38}Ar", PhD thesis, McMaster University, Hamilton, Ontario, Canada (2004)
[20] E. Ideguchi *et al.*, *Phys. Lett.* **B686**, 18 (2010).
[21] D.C. O'Leary *et al., Phys. Rev.* **C61**, 064314 (2000).
[22] A. Bisoi *et al.*, Phys. Rev. C 88, 034303 (2013)
[23] E. Caurier, F. Nowacki, and A. Poves, *Phys. Rev. Lett.* **95**, 042502 (2005).
[24] E. Caurier, J. Menendez, F. Nowacki, and A. Poves, *Phys. Rev.* **C75**, 054317 (2007).
[25] T. Inakura, S. Mizutori, M. Yamagami, and K. Matsuyanagi, *Nucl. Phys.* **A710**, 261 (2002).
[26] R.R. Rodriguez-Guzman, J.L. Egido, and L.M. Robledo, *Int. J. Mod. Phys.* **E13**, 139 (2004).
[27] M. Bender, H. Flocard, and P.H. Heenen, *Phys. Rev.* **C68**, 044321 (2003).
[28] M. Kimura and H. Horiuchi, *Nucl. Phys.* **767**, 58 (2006).
[29] Y. Taniguchi, M. Kimura, Y. Kanada-En'yo, and H. Horiuchi, *Phys. Rev.* **C76**, 044317 (2007).
[30] M. Kimura and H. Horiuchi,*Phys. Rev.* **C69**, 051304 (2004).
[31] Y. Kanada-En'yo and M. Kimura, *Phys. Rev.* **C72**, 064322 (2005).
[32] Y. Taniguchi, Y. Kanada-En'yo, and M. Kimura, *Prog. Theor. Phys.* **121**, 533 (2009).
[33] Y. Taniguchi, Y. Kanada-En'yo, and M. Kimura, *Phys. Rev.* **C80**, 044316 (2009).
[34] K. Hadyńska-Klęk *et al.*, *Phys. Rev. Lett.* **117**, 062501 (2016).
[35] M. Lach *et al.*, *Eur. Phys. J.* **A16**, 309 (2003).
[36] M. Kmiecik *et al.*, *Acta Phys. Pol.* **B36**, 1169 (2005).
[37] K. Hadyńska-Klęk *et al., Acta Phys. Pol.* **B42**, 817 (2011).
[38] K. Hadyńska-Klęk *et al., Acta Phys. Pol.* **B44**, 617 (2013).
[39] D. Cline *Bull. Am. Phys. Soc.* **14**, 726 (1969)
[40] S. Akkoyun *et al.*, *Nucl. Instr. and Meth.* **A668**, 26 (2012)
[41] A. Gadea *et al.*, *Nucl. Instr. and Meth.* **A654**, 88 (2011)
[42] J.J. Valiente-Dobón *et al.*, *Acta Phys. Pol.* **B37**, 225, (2006).
[43] I.J. Thompson, Comput. *Phys. Rep.* 7, 167 (1988).
[44] G. Brown et. al, *Nucl. Phys.* **A 225** 267 (1974)
[45] J. Mierzejewski *et al.*, *Nucl. Instr. and Meth.* **A659**, 84 (2011).
[46] W.J. Kossler *et al.*, *Phys. Rev.* **177** 1725, (1969).
[47] Th. Kern, P. Betz, E. Bitterwolf, F. Glatz, and H. Röpke *Zeit. fur Phys.* **A294**, 51, (1980).
[48] T. Czosnyka, D. Cline, and C.Y. Wu, *Bull. Am. Phys. Soc.* **28**, 745 (1982), www.slcj.uw.edu.pl/gosia
[49] D. Cline, *Annu. Rev. Nucl. Part. Sci.* **36**, 683 (1986).
[50] C.W. Towsley, D. Cline, and R.N. Horoshko, *Nucl. Phys.* **A204**, 574, (1973).
[51] K. Kawade *et al.*, *Jour. Phys. Soc. Japan* **29**, 43, (1970).
[52] P.C. Simms, N. Benczer-Koller, and C.S. Wu, *Phys. Rev.*, **121**, 1169, (1961).
[53] I. Asplund and T. Wiedling, *Phys. Rev.*, **116**, 741, (1959).
[54] W.W. Daehnick and R.D. Rosa, *Phys. Rev.*, **C31**, 1499, (1985)
[55] A.M. Sandorfi, C.J. Lister, D.E. Alburger, and E.K. Warburton, *Phys. Rev.* C22, 2213, (1980).
[56] P.C. Rogers and G.E. Gordon, *Phys. Rev.* **129**, 2653, (1963).
[57] J.W. Nelson, J.D. Oberholtzer, and H.S. Plendl, *Nucl. Phys.* A62, 434, (1965).
[58] R.A. Mendelson and R.T. Carpenter, *Phys. Rev.* **181**, 1552, (1969).
[59] E.K. Warburton, J.J. Kolata, and J.W. Olness, *Phys. Rev.* C11, 700, (1975).
[60] A.R. Poletti *et al.*, *Phys. Rev.* **C10**, 997 (1974).
[61] P. Herges, H.V. Klapdor, and T. Oda, *Nucl. Phys.* **A372**, (1981).
[62] H.H. Eggenhuisen, L.P. Ekström, G.A.P. Engelbertink, and H.J.M. Aarts, *Nucl. Phys.* **A305**, (1978).
[63] R.L. Robinson et al. *Phys. Rev.* **C13**, 1922, (1976).
[64] K.P. Lieb and M. Uhrmacher, *Zeit. fur Phys.* **267**, 399, (1974).
[65] H.L. Scott *et al.*, *Nucl. Instr. and Meth.* **70**, 320, (1968).
[66] A. Jamshidi and W.P. Alford, *Phys. Rev.* **C8**, 1782, (1973).
[67] F. Pellegrini, F. Gentilin, and I. Filosofo, *Phys. Rev.* **C4**, 112, (1971).
[68] S. Cochavi et al., *Phys. Rev.* **C2**, 2241, (1970).

[69] J.D. McCullen and D.J. Donahue, *Phys. Rev.* **C8**, 1406, (1973).

[70] P. Betz *et al.*, *Zeit. fur Phys.* **A276**, 295, (1976).

[71] R. Hartmann *et al.*, *Nucl. Phys.* **123**, 437, (1969).

[72] T. Nomura *et al.*, *Phys. Rev. Lett.* **25**, 1342, (1970).

[73] D.C. Williams, J.D. Knight, and W.T. Leland, Phys. Rev., **164**, 1419, (1967)

[74] F.R. Metzger and G.K. Tandon, *Phys. Rev.*, **148**, 1133, (1966).

[75] P.M. Lewis *et al.*, *Nucl. Phys.* **A** 443, 210, (1985).

[76] M. Marmor, S. Cochavi, and D.B. Fossan, *Phys. Rev. Lett.*, **25**, 1033, (1970).

[77] P.M. Endt and C. van der Leun, *Nucl. Phys.* **214**, 1-625, (1973),

[78] N. Lawley *et al.*, *Nucl. Phys.* **159**, 385, (1970).

[79] M. Marmor *et al.*, *Phys. Rev. Lett.* **25**, 1033, (1970).

[80] A. Winther and J. de Boer, *Coulomb excitation* (Academic Press, New York, 1966) p. 303

[81] R. Hartmann and H. Grawe, *Nucl. Phys.* **164**, 209, (1971).

[82] N.Benczer-Koller, M.Nessin, and T.H.Kruse, *Phys. Rev.*, 123:262 (1961)

[83] H. D. Gräf, H. Feldmeier, P. Manakos, A. Richter and E. Spamer, *Nucl. Phys.* A295 319-332 (1978)

[84] M. Ulrickson, N. Benczer-Koller, J. R. MacDonald and J. W. Tape, *Phys. Rev.* **C16** 186 (1977)

[85] E. Clément *et al.*, *Phys. Rev.* **C94**, 054326 (2016).

[86] M. Zielińska *et al.*, *Eur. Phys. J.* **52**, 99, (2016).

[87] C. Ellegaard *et al.*, *Phys. Lett.* **40B** 641 (1972).

[88] E. Clément *et al.*, *Phys. Rev.* **C75**, 054313 (2007).

[89] H.T. Fortune, *Nucl. Phys.* A962 16 (2017).

[90] J.L. Wood, E.F. Zganjar, C. de Coster, and K. Heyde, Nucl. Phys. **A651**, 323 (1999).

[91] J.P. Davidson, Rev. Mod. Phys. **37**, 105 (1965).

[92] E. Caurier, J. Menendez, F. Nowacki and A. Poves, Phys. Rev. C **75**, 054317 (2007).

[93] R. F. Garcia Ruiz *et al.*,*Phys. Rev.* **C91**, 041304(R) (2015).

[94] E. Caurier, G. Martinez-Pinedo, F. Nowacki, A. Poves and A.P. Zuker, Rev. Mod. Phys. **77**, 427 (2005).

[95] E. Caurier and F. Nowacki, *Acta Phys. Pol.* **B30**, 705 (1999).

[96] A. Bohr, and B. R. Mottelson, K. Dan. Vidensk. Selsk. *Mat. Fys. Medd.* **27**, 16 (1953).

[97] A. S. Davydov and G. F. Filipov, *Nucl. Phys.* **8** 237 (1958).

[98] K. Kumar, *Phys. Rev. Lett.* **28**, 249 (1972).

[99] G. Ripka, Advances in Nuclear Physics, Vol. 1 (Plenum Press, New York, 1968)

[100] B. Bounthong, Ph. D. Thesis, Université de Strasbourg, 2016 (unpublished).

[101] T. R. Rodríguez, and J. L. Egido, Phys. Rev. C 81, 064323 (2010).

[102] J. F. Berger, M. Girod, and D. Gogny, Nucl. Phys. A 428, 23 (1984).

[103] P. Ring, and P. Schuck, *The nuclear many body problem*, Springer-Verlag, Berlin, 1980.

[104] M.Anguiano, J. L. Egido, L.M. Robledo , Nucl. Phys. A 696, 467 (2001).

[105] N. L. Vaquero, T. R. Rodríguez, J. L. Egido, Phys. Lett. B 704, 520 (2011).

[106] M. Borrajo, T. R. Rodríguez and J. L. Egido, Phys. Lett. B 746, 341 (2015).

[107] T. R. Rodríguez, Eur. Phys. J. A, 52, 190 (2016).

[108] J. L. Egido, M. Borrajo, T. R. Rodríguez, Phys. Rev. Lett. 116, 052502 (2016).

[109] F. Q. Chen, J. L. Egido, Phys. Rev. C 95, 024307 (2017).

[110] Y. Taniguchi, *Prog. Theor. Exp. Phys.* **073D01**, (2014).

[111] T. Sakuda, S. Ohkubo, *Phys. Rev.* **C51**, 586 (1995).

[112] T. Wada and H. Horiuchi, Phys. Rev. C 38, 7063 (1988).

[113] T. Sakuda, Prog. Theor. Phys. 87, 1159 (1992).

[114] D. Ray and A. V. Afanasjev, *Phys. Rev.* **C94**, 014310 (2016).

[115] K. Kumar, *Phys. Rev. Lett.* **28**, 249 (1972).

[116] J. Srebrny and D. Cline, *Int. J. Mod. Phys.* **E20**, 422 (2011).

[117] N. Bree *et al.*, *Phys. Rev. Lett.* **112**, 162701 (2014).

[118] K. Wrzosek-Lipska *et al.*, *Phys. Rev.* **C86** 064305 (2012).

[119] J. Srebrny *et al.*, *Nucl. Phys.* **A** 766, 25, (2006).

[120] W. Andrejtscheff and P. Petkov, *Phys. Rev.* **C48**, 2531 (1993).